РОССИЙСКИЙ ГОСУДАРСТВЕННЫЙ ПЕДАГОГИЧЕСКИЙ УНИВЕРСИТЕТ им. А. И. ГЕРЦЕНА
HERZEN STATE PEDAGOGICAL UNIVERSITY of RUSSIA

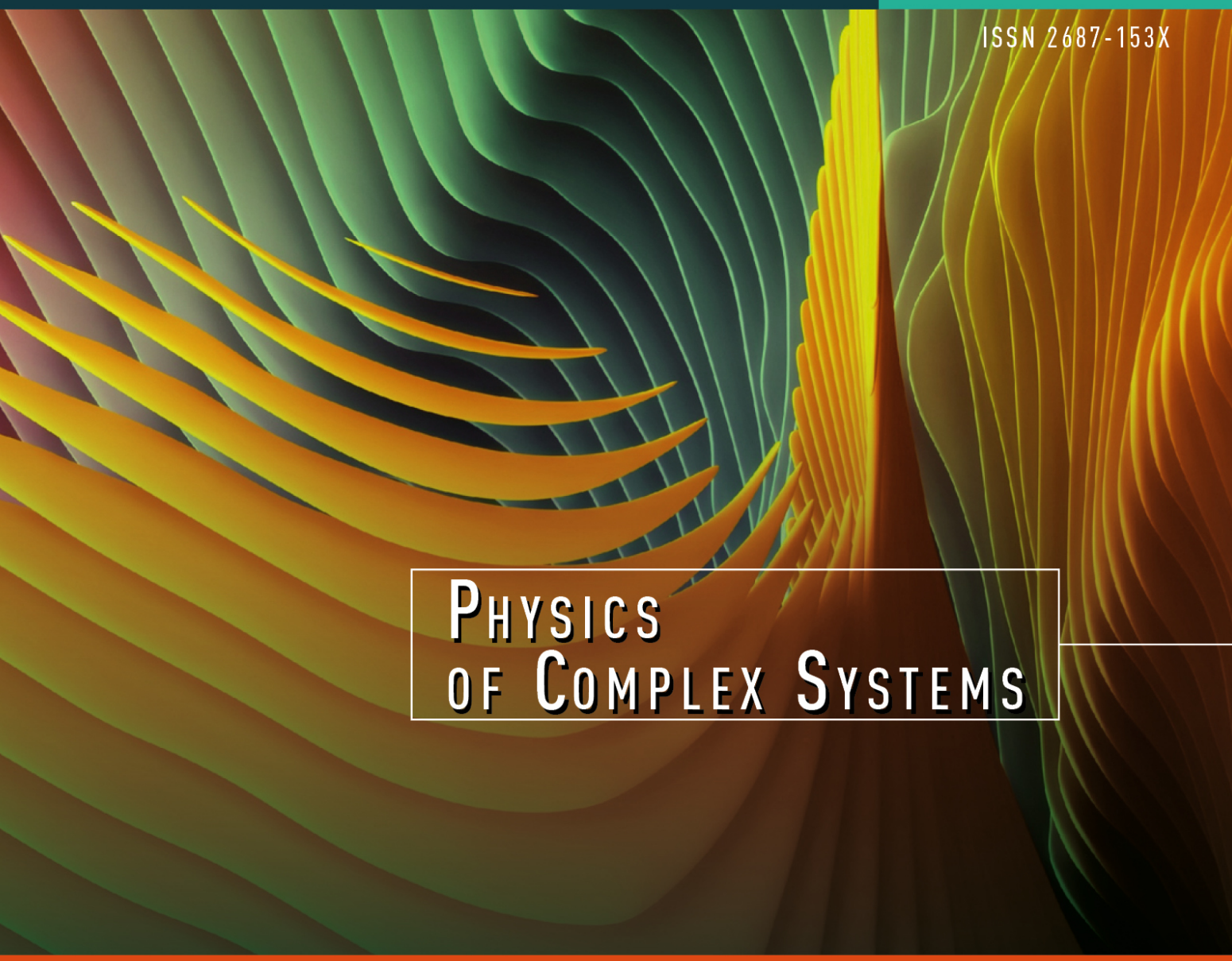

ISSN 2687-153X

Physics of Complex Systems

Т. 3 № 3 2022

Vol. 3 No. 3 2022

Herzen State Pedagogical University of Russia

ISSN 2687-153X (online)
physcomsys.ru
https://www.doi.org/10.33910/2687-153X-2022-3-3
2022. Vol. 3, no. 3

PHYSICS OF COMPLEX SYSTEMS

Mass Media Registration Certificate El No. FS77-77889, issued by Roskomnadzor on 10 February 2020
Peer-reviewed journal
Open Access
Published since 2020
4 issues per year

Publishing house of Herzen State Pedagogical University of Russia
48 Moika Emb., Saint Petersburg 191186, Russia
E-mail: izdat@herzen.spb.ru
Phone: +7 (812) 312-17-41

Data size 3,28 Mbyte
Published at 30.09.2022

Editors of the English text *I. A. Nagovitsyna*
Cover design by *O. V. Rudneva*
Layout by *A. M. Khodan, L. N. Kliuchanskaya*

CONTENTS

Condensed Matter Physics. Dielectrics

UDC 538.9

EDN OCOMWG
https://www.doi.org/10.33910/2687-153X-2022-3-3-104-108

A study of charge relaxation in corona electrets based on P(VDF-TFE) copolymer

Yu. A. Gorokhovatsky[1], Yu. I. Sotova✉[1], D. E. Temnov[1]

[1] Herzen State Pedagogical University of Russia, 48 Moika Emb., Saint Petersburg 191186, Russia

Authors

Yuriy A. Gorokhovatsky, ORCID: 0000-0001-5085-2525, e-mail: gorokh-yu@yandex.ru

Yulia I. Sotova, ORCID: 0000-0001-6792-2390, e-mail: juliasotova1992@mail.ru

Dmitry E. Temnov, ORCID: 0000-0002-9560-4346, e-mail: detem@yandex.ru

For citation: Gorokhovatsky, Yu. A., Sotova, Yu. I., Temnov, D. E. (2022) A study of charge relaxation in corona electrets based on P(VDF-TFE) copolymer. *Physics of Complex Systems*, 3 (3), 104–108. https://www.doi.org/10.33910/2687-153X-2022-3-3-104-108 EDN OCOMWG

Received 20 May 2022; reviewed 6 June 2022; accepted 6 June 2022.

Funding: The research was supported by the Ministry of Education of the Russian Federation as part of the State-Commissioned Assignment, Project No. FSZN-2020-0026.

Abstract. Using the method of thermally stimulated depolarization currents, this paper explains the polarization in the field of corona discharge of polyvinylidene fluoride-tetrafluoroethylene (P(VDF-TFE)) copolymer films. It has been determined that to achieve the best electret properties of PVDF, polarization must be carried out in the field of negative corona discharge. It was found that the studied objects have two types of polar structures different in the activation energy and the frequency factor. Using a mix of traditional and numerical methods to analyze the peaks of the thermally stimulated depolarization currents, the parameters of the polar structures of both types found in P(VDF-TFE) were determined.

Keywords: electret state, polyvinylidene fluoride, tetrafluoroethylene, piezoelectric effect, TSD spectroscopy, weak regularization method

Introduction

Polymer films based on polyvinylidene fluoride (PVDF) and its copolymers with trifluoroethylene P(VDF-TrFE) and tetrafluoroethylene P(VDF-TFE) are widely used in electroacoustic transducers (in particular, in hydrophones) due to their piezoelectric properties (Aguilar et al. 2021; Martins et al. 2019).

PVDF is a semicrystalline polymer. The crystalline phase exhibits polymorphism and exists in five different crystalline modifications: α-, β-, γ-, δ- and ε-phases (Begum et al. 2018). The polar β-phase has piezoelectric properties (Kalimuldina et al. 2020). However, researchers still do not share a common ground regarding the nature of piezoelectricity in PVDF.

One of the most common ways to create a piezoelectric state in PVDF-based films is polarization in corona discharge field at an elevated temperature. The popularity of this method is due to the fact that corona polarization (compared to contact polarization) results in higher field values (Sukumaran et al. 2021). In this case, in addition to the piezoelectric state, an electret state is also formed in PVDF (Wang et al. 2016).

The reported study investigated the formation of the electret state in P(VDF-TFE) films.

Samples and research methods

The object of the study was a P(VDF-TFE) copolymer film (F2ME, 20 μm thick, mechanically stretched). A piezoelectric state was created in the samples using corona discharge field under special polarization conditions: the sample was placed in corona discharge field for 10 min (keeping the temperature constant) and then cooled to room temperature in this field. It is known that the magnitude of the electric field strength to form a piezoelectric state in PVDF is 1.2 MV/cm (Mahadeva et al. 2013). The value of the polarization temperature varied from 50 °C to 80 °C.

To study the accumulation of charges and relaxation occurring in P(VDF-TFE) during polarization, the method of thermally stimulated depolarization currents (TSD) was used. TSD measurements were carried out on a TSC II installation by Setaram.

Experimental results and discussion

Fig. 1 shows TSD curves in P(VDF-TFE) films polarized in the fields of negative and positive corona discharges (in both cases the polarization temperature was 70 °C).

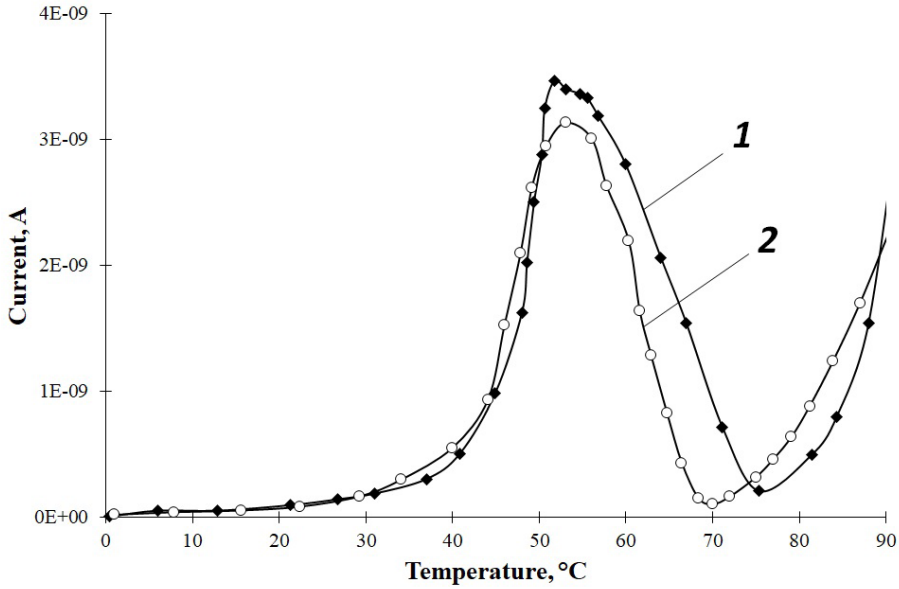

Fig. 1. Thermally stimulated depolarization currents in P(VDF-TFE) films polarized in the field of negative (1) and positive (2) corona discharge (polarization temperature is 70 °C)

TSD curves in Fig. 1 show a peak that is identical in its temperature position (about 50 °C) for both corona electrode polarities. However, the beginning and nature of an increase in current above 70 °C strongly depends on the corona electrode polarity: for positive polarity, the increase begins earlier and is less steep than for the negative polarity.

Apparently, when the film is polarized in the field of corona discharge, the homocharge (positive or negative) is captured by deep near-surface traps. The homocharge itself does not contribute to the piezoelectric state in P(VDF-TFE), however, in the resulting internal electric field of the homocharge, the oriented state of the polar structures (present in the piezoelectric β-phase of PVDF) is maintained, which is essential for maintaining the piezoelectric state. On the TSD curves, the misorientation of the polar structures is shown as a peak near 50 °C (therefore, its temperature position does not depend on the polarity of the corona electrode), and the release of the homocharge from deep surface traps is shown as an increase in current at above 70 °C.

It is possible to estimate the value of the homocharge activation energy by the initial rise method (Gorokhovatskiy, Bordovskiy 1991). The obtained value is (1.90 ± 0.09) eV for negative electrode polarity and (1.20 ± 0.06) eV for positive electrode polarity. Thus, the trap depth for a negative homocharge is greater than for a positive one, and to achieve the best electret properties of PVDF, polarization must be carried out in the field of negative corona discharge.

Fig. 2 shows TSD curves in P(VDF-TFE) films polarized in the field of negative corona discharge at different polarization temperatures. It can be seen from the obtained data that at a low polarization temperature (50–60 °C), the TSD curves exhibit one peak in the region of 50 °C, and with an increase in the polarization temperature (70 °C and 80 °C), the curves show two strongly overlapping peaks (at around 40–70 °C).

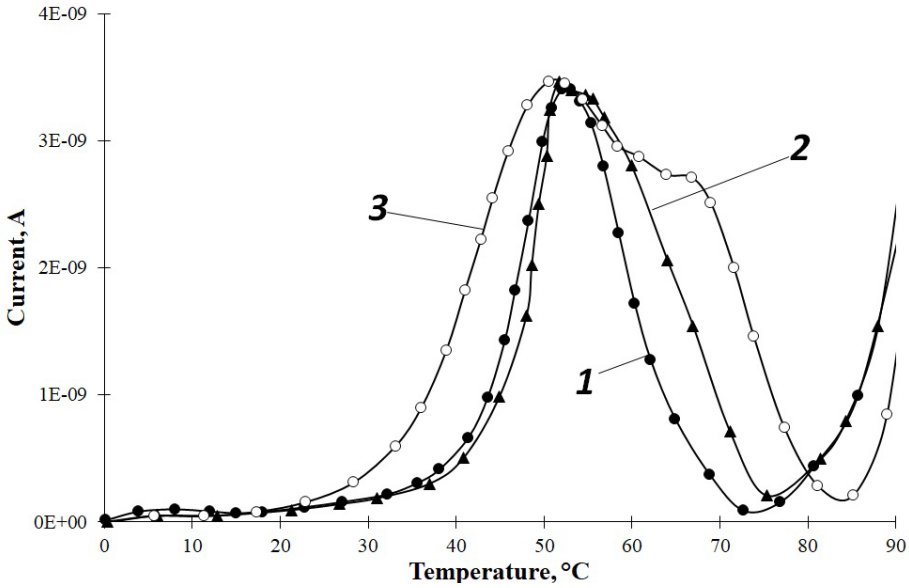

Fig. 2. Thermally stimulated depolarization currents in P(VDF-TFE) films polarized in the field of negative corona discharge at different polarization temperatures: 50 °C (1), 70 °C (2), and 80 °C (3)

Apparently, there are two kinds of polar structures in P(VDF-TFE) with different activation energies. During polarization in the field of corona discharge at a temperature of 50–70 °C, in the internal electric field of a homocharge, polar structures of only one type are oriented (with a lower activation energy shown as the current peak at around 50 °C). An increase in the polarization temperature to 80 °C leads to the orientation of both types of polar structures shown as the appearance of two strongly overlapping peaks on the TSD curves (in the temperature range from 40 °C to 70 °C).

The method of varying the heating rate was used to estimate the value of the activation energy and the frequency factor of polar structures with a lower activation energy (Gorokhovatskiy, Bordovskiy 1991). Table 1 shows the results of calculating the activation energy and the frequency factor (with an accuracy of half a decade) of polar structures present in the composition of P(VDF-TFE) polarized at different polarization temperatures.

Table 1. Values of the activation energy and frequency factor (with an accuracy of half a decade) of polar structures with a lower activation energy in P(VDF-TFE) films polarized at different polarization temperatures

Polarization temperature	Activation energy W, eV	Frequency factor ω, sec.$^{-1}$
50 °C	0.84 ± 0.03	10^{10}
70 °C	0.83 ± 0.03	10^{10}
80 °C	0.83 ± 0.03	10^{10}

Due to a too strong overlap of two closely spaced peaks, traditional methods for calculating the frequency factor and the activation energy are not effective enough for the estimation of these parameteres in the case of polar structures with a higher activation energy. In this case, Tikhonov's numerical method of weak regularization can be used (Gorokhovatsky et al. 2018). Based on the experimental temperature dependence of the TSD currents, it is possible, using numerical methods, to restore the distri-

 https://www.doi.org/10.33910/2687-153X-2022-3-3-104-108

bution function of relaxing structures (in our case, polar structures) *G(W)* with respect to the activation energy. As a result, the obtained parameter values are W = (0.83 ± 0.04) eV, ω 10^{10} $sec.^{-1}$ for polar structures with lower activation energy and W = (0.89 ± 0.04) eV, $\omega = 10^{11}$ $sec.^{-1}$ for polar structures with higher activation energy (the frequency factor is determined with an accuracy of half a decade). It turns out that the polar structures in P(VDF-TFE) differ not only in the value of the activation energy, but also in the value of the frequency factor. Fig. 3 shows the distribution function of polar structures in P(VDF-TFE) *G(W)* in terms of activation energy for two types of polar structures (taking into account the difference in the value of the frequency factor).

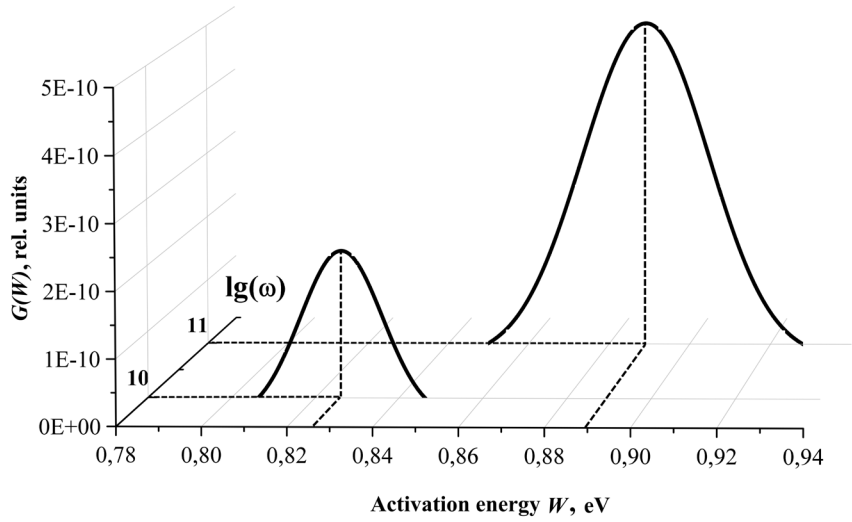

Fig. 3. The distribution function of polar structures in P(VDF-TFE) *G(W)* in terms of activation energy for the two types of polar structures (taking into account the difference in the value of the frequency factor)

Thus, the complex application of traditional methods for processing TSD current peaks and Tikhonov's numerical method of weak regularization made it possible to find the parameters of the polar structures of both types present in P(VDF-TFE).

Conclusions

Using thermal activation spectroscopy, the mechanism of polarization in P(VDF-TFE) copolymer films was identified: during polarization in the corona discharge field, deep near-surface traps capture a homocharge. In the internal homocharge electric field, the polar structures are oriented and their oriented state is maintained. An increase in the polarization temperature increases the contribution of dipoles with a higher activation energy (which is observed in the TSD curves as two strongly overlapping peaks). The activation energies of polar structures of two different types are (0.82 ± 0.03) eV and (0.89 ± 0.04) eV, frequency factors are 10^{10} $sec.^{-1}$ and 10^{11} $sec.^{-1}$ (accurate to half a decade). The depth of traps for positive and negative homocharge is different and amounts to (1.20 ± 0.09) eV and (1.90 ± 0.09) eV, respectively.

Conflict of Interest

The authors declare that there is no conflict of interest, either existing or potential.

Author Contributions

The authors have made an equal contribution to the preparation of the text.

References

Aguilar, J. Q., Álvarez-Arenas, T. G., Svilainis, L. (2021) Ferroelectret hydrophone. In: *2021 IEEE International Ultrasonics Symposium (IUS)*. Xi'an: IEEE Publ., pp. 1–4. https://doi.org/10.1109/IUS52206.2021.9593895 (In English)

Begum, S., Ullah, H., Kausar, A. et al. (2018) Fabrication of epoxy functionalized MWCNTs reinforced PVDF nanocomposites with high dielectric permittivity, low dielectric loss and high electrical conductivity. *Composites Science and Technology*, 167, 497–506. https://doi.org/10.1016/j.compscitech.2018.08.041 (In English)

Gorokhovatskiy, Yu. A., Bordovskiy, G. A. (1991) *Termoaktivatsionnaya tokovaya spektroskopiya vysokoomnykh poluprovodnikov i dielektrikov [Thermal activation spectroscopy of high-resistance semiconductors and dielectrics]*. Moscow: Nauka Publ., 244 p. (In Russian)

Gorokhovatsky, Yu. A., Temnov, D. E., Sotova, Yu. A. et al. (2018) Thermally stimulated depolarization data analysis: Simmons method and weak regularization method by Tikhonov. *Universitetskij Nauchnyj Zhurnal — University Scientific Journal*, 37, 40–48. (In English)

Kalimuldina, G., Turdakyn, N., Abay, I. et al. (2020) A review of piezoelectric PVDF film by electrospinning and its applications. *Sensors*, 20 (18), article 5214. https://doi.org/10.3390/s20185214 (In English)

Mahadeva, S. K., Berring, J., Walus, K., Stoeber, B. (2013) Effect of poling time and grid voltage on phase transition and piezoelectricity of poly(vinyledene fluoride) thin films using corona poling. *Journal of Physics D: Applied Physics*, 46 (28), article 285305. https://doi.org/10.1088/0022-3727/46/28/285305 (In English)

Martins, M. S., Faria, C. L., Matos, T. et al. (2019) Performance evaluation of a PVDF hydrophone for deep sea applications. *OCEANS 2019—Marseille*. Marseille: IEEE Publ., pp. 1–5. https://doi.org/10.1109/OCEANSE.2019.8867156 (In English)

Sukumaran, S., Chatbouri, S., Rouxel, D. et al. (2021) Recent advances in flexible PVDF based piezoelectric polymer devices for energy harvesting applications. *Journal of Intelligent Material Systems and Structures*, 32 (7), 746–780. https://doi.org/10.1177/1045389X20966058 (In English)

Wang, S., Zhao, X., Yin, X. et al. (2016) Electret polyvinylidene fluoride nanofibers hybridized by polytetrafluoroethylene nanoparticles for high-efficiency air filtration. *ACS Applied Materials & Interfaces*, 8 (36), 23985–23994. https://doi.org/10.1021/acsami.6b08262 (In English)

Condensed Matter Physics. Dielectrics

UDC 537.3

EDN PTWGYL
https://www.doi.org/10.33910/2687-153X-2022-3-3-109-116

Gas discharge activation of new poly(lactic acid) packaging composite films

A. A. Pavlov✉[1], A. M. Kamalov[1], M. E. Borisova[1], K. V. Malafeev[2], V. E. Yudin[2]

[1] Peter the Great St. Petersburg Polytechnic University, 29 Polytechnicheskaya Str., Saint Petersburg 195251, Russia
[2] Institute of Macromolecular Compounds RAS, 31 Bolshoy Ave., Saint Petersburg 199004, Russia

Authors

Andrey A. Pavlov, ORCID: 0000-0001-5459-7509, e-mail: pavlov.aa.hv@mail.ru

Almaz M. Kamalov, ORCID: 0000-0003-2044-957X, e-mail: spb.kamalov@gmail.com

Margarita E. Borisova, ORCID: 0000-0003-0761-6302, e-mail: vladimirl.borisov@gmail.com

Konstantin V. Malafeev, ORCID: 0000-0002-8540-8608, e-mail: kostya_malafeev@mail.ru

Vladimir E. Yudin, ORCID: 0000-0002-5517-4767, e-mail: yudin@hq.macro.ru

For citation: Pavlov, A. A., Kamalov, A. M., Borisova, M. E., Malafeev, K. V., Yudin, V. E. (2022) Gas discharge activation of new poly(lactic acid) packaging composite films. *Physics of Complex Systems*, 3 (3), 109–116. https://www.doi.org/10.33910/2687-153X-2022-3-3-109-116 EDN PTWGYL

Received 12 May 2022; reviewed 6 June 2022; accepted 6 June 2022.

Funding: The research was funded by the Grant for young scientists (Ministry of Education and Science) MK-4346.2022.4

Abstract. This work focuses on new poly(lactic acid) electroactive packaging composite films with different mass percentages of a filler. Hydroxyapatite (HA), Poviargolum (PA) and vapor-grown carbon fibers (VGCF) were used as fillers. The films were produced by extrusion. Mechanical, electric and electretic properties were studied. Time dependences of the electretic potential differences were identified. The properties of the samples were compared and the most suitable films (0.5% HA, 5% PA, 0.5% VGCF) were chosen.

Keywords: polylactide, electret, composite material, hydroxyapatite, Poviargolum, vapor-grown carbon nanofibers

Introduction

In recent years, polymers have become an essential part of our life. Their outstanding mechanical and electrical properties make them irreplaceable in many industries. Mass production of petroleum-based polymers leads to a problem with their disposal, e. g., polyethylene breakdown in the natural environment can take several hundreds of years. A possible solution to this issue is biodegradable materials.

Made from lactic acid, polylactide (PLA) is one of the most popular biodegradable polymers (Fig. 1). It can quickly break down in a special compost, leaving only carbon dioxide, water and other harmless substances (Valdes et al. 2014; Yu et al. 2006). PLA is widely used as a material for 3D printing, surgical threads (due to its high biocompatibility) and food packaging (Cabedo et al. 2006; Garlotta 2001).

Another growing trend is the usage of active packaging. Electroactive polymer materials have bactericidal qualities, which positively affect the shelf life of a product. Dielectrics that provide such qualities due to a static electric field are called electrets (Borisova, Kojkov 1979). Polylactide has poor electretic properties (Guzhova 2016; Urbaniak-Domagala 2013). Thus, the goal of this work was to develop new PLA-based composite material and identify the optimal mass percentage of each filler with the best electretic properties.

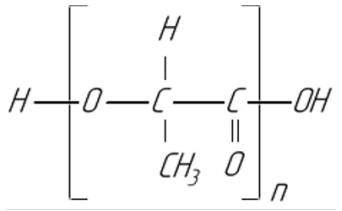

Fig. 1. The structural formula of PLA

Materials and methods

To improve the electretic properties of PLA, hydroxyapatite (HA), Poviargolum (PA) and vapor-grown carbon fibers (VGCF) were added as fillers. Two types of PLA matrix were used: PURAC PL18 (100% L-lactide) and Nature Works PLA 2003D (96% L-lactide, 4% D-lactide). The latter was used in composites with the addition of PA. The film samples were produced in the Institute of Macromolecular Compounds RAS. PLA and fillers were mixed in a double-screw microextruder DSM Xplore.

Hydroxyapatite is a mineral form of calcium apatite. Being a major component of human bones and dental enamel, it is frequently used in dentistry and fracture treatments. The mass percentage of hydroxyapatite in the composites varied from 0% to 3% (0%, 0.5%, 1%, 1.5%, 3%).

Poviargolum is a highly dispersed silver stabilized with polyvinylpyrrolidone (PVP). The silver to PVP ratio is approximately 8/92. Due to its antiseptic properties, it is often used in clinical practice. The mass percentage of Poviargolum varied from 1% to 5% (1 and 5%).

Vapor-grown carbon fibers (VGCF) have great mechanical properties. They are frequently used in composite materials to improve their electrical and thermal conductivity. The mass percentage of VGCF varied from 0.5% to 5% (0.5%, 1%, 3%, 5%).

A corona discharge was used to create an electret state in the samples (Borisova, Kamalov 2016). This is a widely spread method of electret production, which does not require any special equipment or environmental conditions. The compensation method with a vibrating electrode was used to measure the surface potential of an electret, as in our previous work (Pavlov et al. 2020). The goal was to conduct a one-week test to determine the most suitable samples. This period was chosen deliberately: most foods do not last longer than a week.

There are two mechanisms of charge relaxation in polymer dielectrics. It can occur due to the charge carriers moving through the sample (the intrinsic conductivity theory), or due to the charge carriers being released from the traps (the dispersion transport theory). Using the acquired time dependences of the electretic potential differences, the prevailing mechanism in each sample can be determined.

According to the intrinsic conductivity theory, the conductivity of the sample (γ) can be achieved using (1) (Borisova et al. 2004):

$$\gamma = -\varepsilon\varepsilon_0 \frac{dU}{dt} \tag{1}$$

The dispersion transport theory suggests that a dielectric material is ideal ($\gamma = 0$). The charge carrier mobility can be determined using the following formulas (Borisova 2014), where h is the thickness of the sample and μ is the charge carrier mobility ($m^2/(V^*s)$).

$$\mu(t) = -2\frac{h^2}{U^2(t)} \times \frac{dU(t)}{dt}, t \le t_\lambda \tag{2}$$

$$\mu(t) = -\frac{h^2}{2U^2(t)} \times \frac{dU(t)}{dt}, t \ge t_\lambda \tag{3}$$

$$U(t_\lambda) = \frac{U(0)}{2} \tag{4}$$

The prevailing relaxation mechanism can be assumed by comparing the achieved $\mu(t)$ and $\gamma(t)$ curves and using (5), where n is the quantity of electrons and e is the elementary charge.

$$\gamma = ne\mu \tag{5}$$

 https://www.doi.org/10.33910/2687-153X-2022-3-3-109-116

If the curves have similar shapes, then we can suggest that the dispersion transport mechanism is prevailing in the sample.

The developed materials should be at least as durable as the original PLA matrix in order to be suitable for use in packaging. The mechanical properties of the film samples were investigated when they were stretched on an Instron 5943 tensile testing machine. The basic length of the test samples was 30 mm, width 4 mm, thickness about 20 μm. The stretching speed was 5 mm/min.

Results and discussion

The first test was 1 hour long. It helped to determine the most stable samples. The charging time for each sample was 60 seconds (at room temperature); the surface potential reached 500 V.

Fig. 2 shows the time dependences of the electretic potential differences of the samples with different mass value of HA (0%, 0.5%, 1%, 1.5%, 3%).

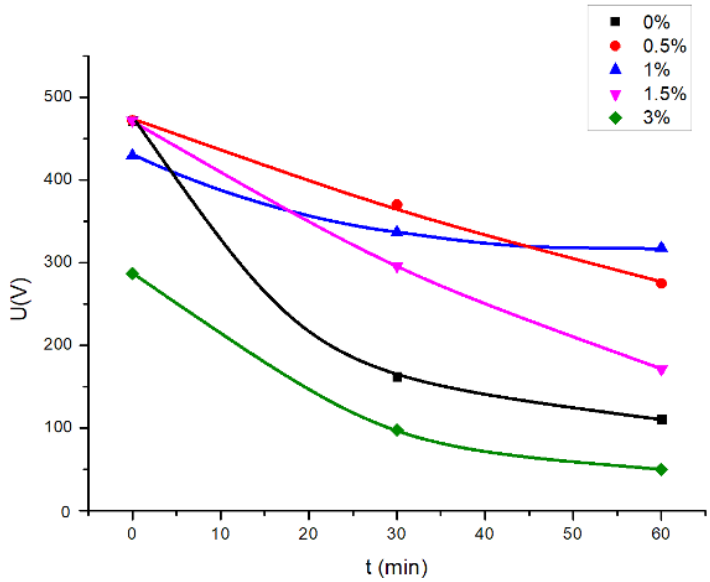

Fig. 2. Time dependences of the electretic potential differences of the samples with HA (0%, 0.5%, 1%, 1.5%, 3%)

The plot suggests that samples with 0.5% and 1% HA preserve the charge better compared to the other samples. The samples with 0%, 1.5% and 3% HA fully discharged the next day.

The charged samples with PA and VGCF were put to the same test (Fig. 3).

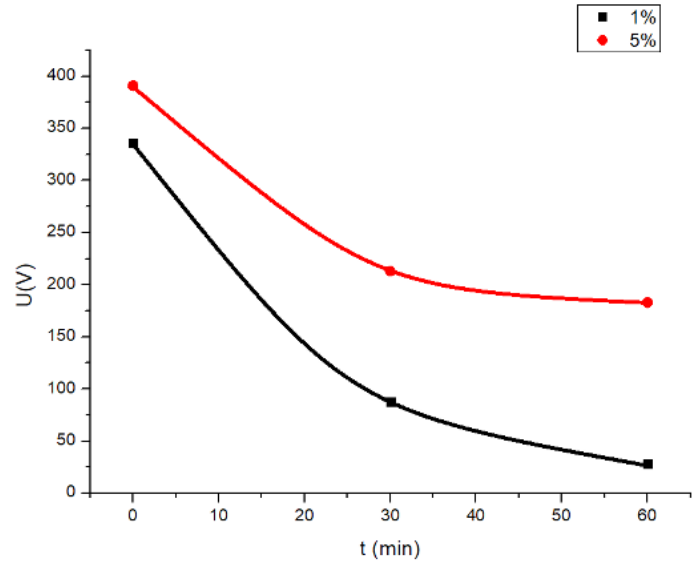

Fig. 3. Time dependences of the electretic potential differences of the samples with PA (1%, 5%)

The sample with 1% PA fully discharged the next day (Fig 4).

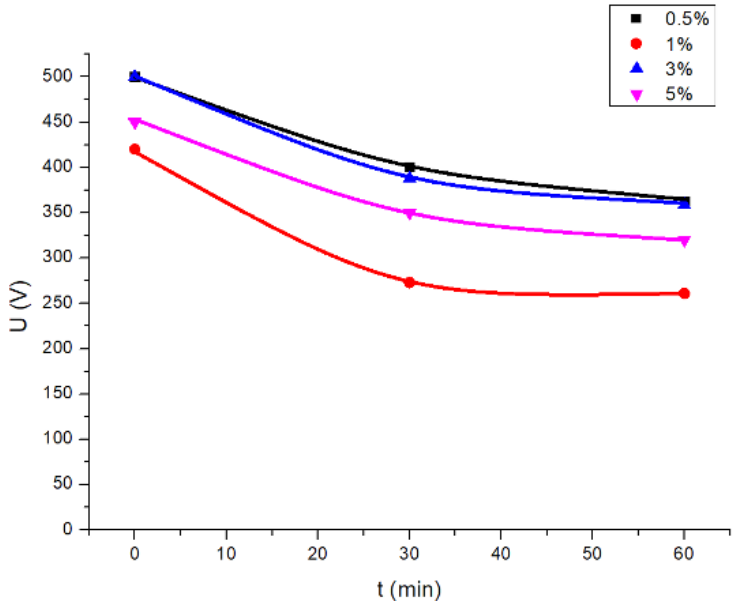

Fig. 4. Time dependences of the electretic potential differences of the samples with VGCF (0.5%, 1%, 3%, 5%)

The plot suggests that all samples with VGCF have good charge preservation capability.

The second test was one week long and was conducted upon the chosen samples from the former test.

Fig. 5 shows the time dependences of the electretic potential differences of the samples with HA (0.5%, 1%) and PA (5%).

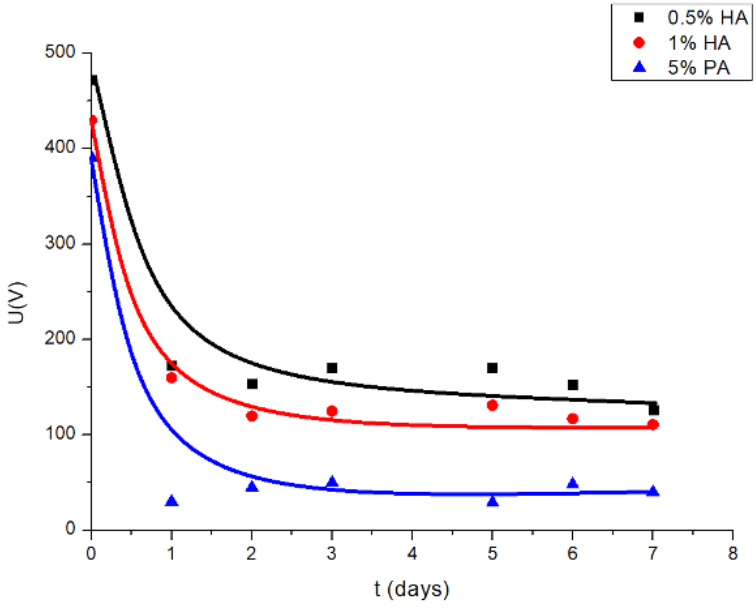

Fig. 5. Time dependences of the electretic potential differences of the samples with HA (0.5%, 1%) and PA (5%)

https://www.doi.org/10.33910/2687-153X-2022-3-3-109-116

Using the plot, we can assume that the optimal mass value of HA is 0.5%.
The sample with 0.5% VGCF seems to have the longest charge relaxation time (Fig. 6).

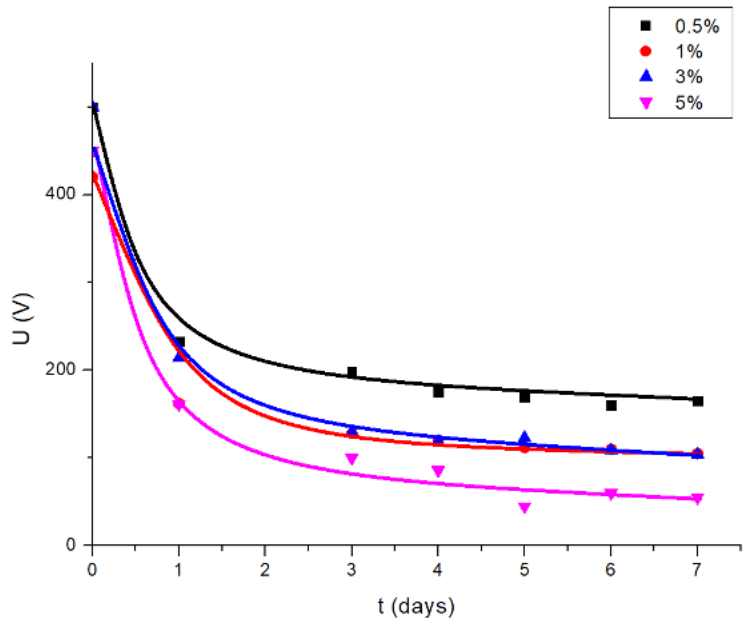

Fig. 6. Time dependences of the electretic potential differences of the samples with VGCF (0.5%, 1%, 3%, 5%)

The speed of discharge can be compared using the time period when the electretic potential difference is one half of the initial (Pavlov et al. 2021): 24 h for the samples with 0.5% HA and 5% PA, 30 h for the 0.5% VGCF sample, 45 min for the original PLA sample.

The intrinsic conductivity (Fig. 7) and the charge carrier mobility (Fig. 8) were calculated for the remaining samples (0.5% HA, 5% PA, 0.5% VGCF).

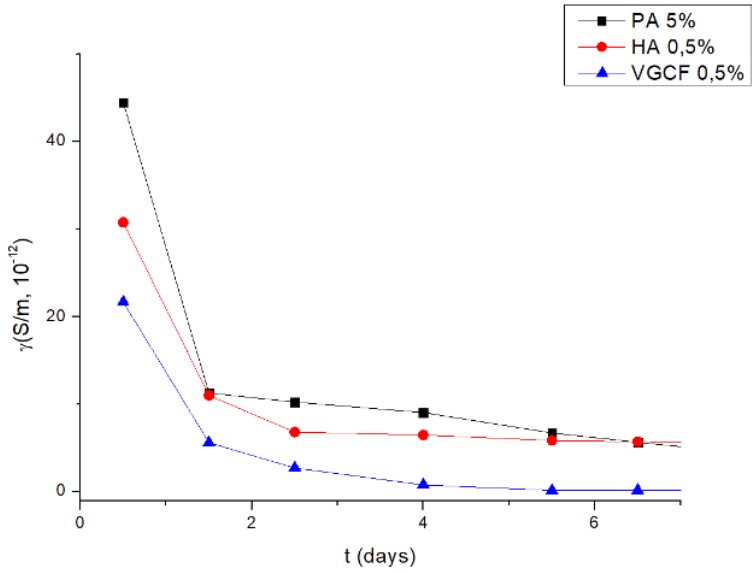

Fig. 7. Time dependences of the intrinsic conductivity of the samples with 0.5% HA, 5% PA and 0.5% VGCF

These exponential curves are characteristic for polymer dielectrics.

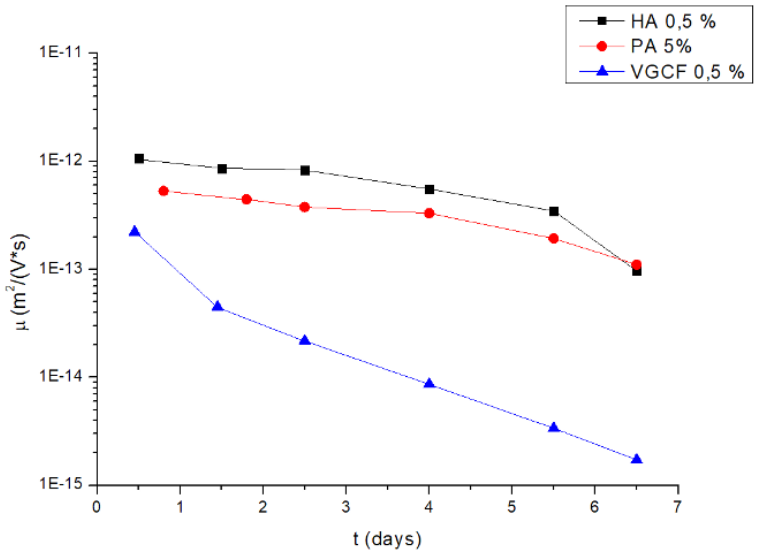

Fig. 8. Time dependences of the charge carrier mobility of the samples with 0.5% HA, 5% PA and 0.5% VGCF

Comparing the curves in Fig. 7 and Fig. 8 and using (5), we assume that charge relaxation in the sample with 0.5% VGCF mostly occurs according to the dispersion transport theory. In the samples with HA and PA the charge carrier mobility does not change much, so it might be suggested that the intrinsic conductivity of these samples is the main reason for charge relaxation.

The mechanical properties of the film samples are shown in Table 1, Table 2, and Table 3.

Table 1. Mechanical properties of HA samples

Properties	**Samples**				
	PL18	**0.5%**	**1%**	**1.5%**	**3%**
Strength, MPa	41 ± 3	40 ± 3	25 ± 3	30 ± 4	19 ± 3
Elastic modulus, GPa	1.8 ± 0.2	1.9 ± 0.2	1.5 ± 0.1	1.6 ± 0.2	1.4 ± 0.2
Deformation before rupture, %	6 ± 1	6 ± 1	8 ± 1	7 ± 1	6 ± 3

Table 2. Mechanical properties of PA samples

Properties	**Samples**		
	PLA	**1%**	**5%**
Strength, MPa	26 ± 3	25 ± 2	24 ± 2
Elastic modulus, GPa	1.6 ± 0.4	1.6 ± 0.2	1.7 ± 0.2
Deformation before rupture, %	6 ± 1	10 ± 7	12 ± 7

https://www.doi.org/10.33910/2687-153X-2022-3-3-109-116

Table 3. Mechanical properties of VGCF samples

Properties	Samples				
	PL18	0.5%	1%	3%	5%
Strength, MPa	41 ± 3	41 ± 4	44 ± 1	38 ± 5	25 ± 3
Elastic modulus, GPa	1.8 ± 0.2	1.6 ± 0.3	1.6 ± 0.3	1.5 ± 0.2	1.3 ± 0.1
Deformation before rupture, %	6 ± 1	33 ± 6	26 ± 6	20 ± 3	16 ± 3

Table 1 shows that with an increase in the concentration of HA, the strength gradually decreases. With the addition of 1% HA the strength drops to 25 MPa. It should also be noted that the addition of HA does not affect the values of the modulus of elasticity and the deformation before rupture.

The films with the addition of Poviragolum were made from packaging PLA, so the strength values differ. Table 2 shows that Poviargolum does not affect the strength and the elastic modulus of the films. They remain at 25 MPa and 1.4 GPa respectively. The changes in the deformation before rupture of the films are at the same level.

The addition of VGCF significantly increases the deformation before rupture of the films. The strength and the elastic modulus of the samples gradually decrease with the further addition of the filler.

The addition of 0.5% HA and 5% PA has almost no effect on the mechanical properties of a composite, which makes them suitable for use in food packaging. The addition of 0.5% VGCF makes the value of the deformation before rupture 5 times greater; this may be explained by the high dispersive ability of fibers. This sample is the optimal choice due to its superior electretic and mechanical properties.

Conclusion

The optimal mass percentage of each filler to produce the best electretic properties was found (0.5% HA, 5% PA, 0.5% VGCF). The addition of each filler creates new charge traps in the PLA matrix, which increase charge relaxation time. The stability of the electret state in the developed composite materials showed a ten times increase.

The mechanisms of charge relaxation in the samples were determined (intrinsic conductivity for the samples with HA and PA, dispersion transport for the PLA + VGCF samples); the mechanical properties of the film samples were investigated. Based on the obtained results, the chosen samples are seen to have suitable properties for their use in active packaging and can be recommended for practical testing.

Conflict of Interest

The authors declare that there is no conflict of interest, either existing or potential.

Author Contributions

Andrey A. Pavlov, Almaz M. Kamalov and Margarita E. Borisova developed the concept, conducted the study, wrote the original draft and managed the project.

Konstantin V. Malafeev and Vladimir V. Yudin conducted the study, reviewed and edited the article.

References

Borisova, M. E. (2014) *Fizika dielektrikov. Fizicheskie osnovy aktivnykh dielektrikov [Physics of dielectrics. Physical fundamentals of active dielectrics]*. Saint Petersburg: Polytechnic University Publ., 121 p. (In Russian)

Borisova, M. E., Galyukov, O. V., Tsatsynkin, P. V. (2004) *Fizika dielektricheskikh materialov. Elektroperenos i nakoplenie zaryada v dielektrikakh [Physics of dielectric materials. Charge transfer and preservation in dielectrics]*. Saint-Petersburg: Saint Petersburg State University Publ., 106 p. https://doi.org/10.18720/SPBPU/2/si20-477 (In Russian)

Borisova, M., Kamalov, A. M. (2016) Specific of electret state of modified polyimide films. In: *57th International Scientific Conference on Power and Electrical Engineering of Riga Technical University*. Riga: IEEE Publ., pp. 1–4. https://doi.org/10.1109/RTUCON.2016.7763095 (In English)

Borisova, M. E, Kojkov, S. N. (1979) *Fizika dielektrikov [Physics of dielectrics]*. Leningrad: Leningrad State University Publ., 240 p. (In Russian)

Cabedo, L., Feijoo, J. L., Villanueva, M. et al. (2006) Optimization of biodegradable nanocomposites based on a PLA/PCL blends for food packaging applications. *Macromolecular Symposia*, 233 (1), 191–197. https://doi.org/10.1002/masy.200690017 (In English)

Garlotta, D. (2001) A literature review of poly(lactic acid). *Journal of Polymers and the Environment*, 9 (2), 63–84. https://doi.org/10.1023/A:1020200822435 (In English)

Guzhova, A. A. (2016) *Elektretnye kompozitsionnye materialy na osnove polilaktida [Electret composite materials based on polylactide]. PhD dissertation (Polymer and Composite Materials)*. Kazan, Kazan National Technological Research University, 132 p. (In Russian)

Pavlov, A. A., Kamalov, A. M., Borisova, M. E. et al. (2021) The study of the charge relaxation kinetics in polyethylene with nanofillers. *Journal of Physics: Conference Series*, 2103, article 012104. https://doi.org/10.1088/1742-6596/2103/1/012104 (In English)

Pavlov, A., Borisova, M., Kamalov, A. et al. (2020) The effect of hydroxyapatite on the electrical properties of a polylactide-based composite. In: *2020 IEEE Conference of Russian young researchers in electrical and electronic engineering (EIConRus)*. Moscow; Saint Petersburg: IEEE Publ., pp. 1042–1044. https://doi.org/10.1109/EIConRus49466.2020.9039381 (In English)

Urbaniak-Domagala, W. (2013) Electrical properties of polylactides. *Journal of Electrostatics*, 71 (3), 456–461. https://doi.org/10.1016/j.elstat.2013.01.008 (In English)

Valdes, A., Mellinas, A. C., Ramos, M. et al. (2014) Natural additives and agricultural wastes in biopolymer formulations for food packaging. *Frontiers in Chemistry*, 2, article 6. https://doi.org/10.3389/fchem.2014.00006 (In English)

Yu, L., Dean, K., Li, L. (2006) Polymer blends and composites from renewable resources. *Progress in Polymer Science*, 31 (6), 576–602. https://doi.org/10.1016/j.progpolymsci.2006.03.002 (In English)

Theoretical physics. Cosmology

UDC 524.8

EDN PYVSES
https://www.doi.org/10.33910/2687-153X-2022-3-3-117-121

The forces outside the static limit in the rotating frame

A. A. Grib✉[1], V. D. Vertogradov[1], I. E. Fedorov[1]

[1] Herzen State Pedagogical University of Russia, 48 Moika Emb., Saint Petersburg 191186, Russia

Authors

Andrey A. Grib, ORCID: 0000-0002-6389-991X, e-mail: andrei_grib@mail.ru

Vitalii D. Vertogradov, ORCID: 0000-0002-5096-7696, e-mail: vdvertogradov@gmail.com

Ivan E. Fedorov, e-mail: fedivan97@gmail.com

For citation: Grib, A. A., Vertogradov, V. D., Fedorov, I. E. (2022) The forces outside the static limit in the rotating frame. *Physics of Complex Systems*, 3 (3), 117–121. https://www.doi.org/10.33910/2687-153X-2022-3-3-117-121 EDN PYVSES

Received 15 March 2022; reviewed 25 March 2022; accepted 6 April 2022.

Funding: This study was supported by grant No. 22-22-00112 RSF. It was also part of the SAO RAS state assignment Fundamental Scientific Research.

Abstract. This paper focuses on the rotating frame of the Minkowski spacetime to describe the inertial forces outside the static limit. We consider the inertial forces inside the static limit to find the classical analogue. Then, we find out the expressions for these forces outside the static limit where we cannot consider the limit $\frac{v}{c} \to 0$. We show that, generaly, if the angular velocity of the object Ω is equal to the angular momentum ω, then the acceleration is equal to zero. When $\omega \neq \Omega$, we show that $\omega - \Omega$ is a decreasing function of r.

Keywords: rotating frame, static limit, inertial force, geodesic, Minkowski spacetime

Introduction

The focus on rotating black holes led the authors of (Grib, Pavlov 2019) to conclude that ergosphere, geodesics with negative energies, and the Penrose effect (Grib, Pavlov 2011; Grib et al. 2014; Vertogradov 2015) are typical not only for black holes but also for the Minkowski spacetime in rotating coordinates. It was shown that the role of the static limit in the theory of rotating black holes is taken by the distance from the origin of rotating coordinates to the value of the radius where the linear velocity of rotation becomes equal to the speed of light. The region beyond this value plays the role of ergosphere. In this region all bodies must be moving. This corresponds to use of the rotating rods and presents the main difference from observations inside the limit where all bodies can be at rest. In this paper we consider the geodesic lines both inside and outside the static limit in rotating coordinates. This is done to initiate the discussion of the inertial forces appearing in these coordinates in the Minkowski spacetime. These forces inside the limit are well-known centrifugal and Coriolis forces. The analogues of these forces for the region outside the static limit are presented in this paper.

In the paper (Grib, Pavlov 2019) authors showed that the analogue of the Penrose effect outside the static limit can lead to observational effects inside this static limit. The study reported in this paper is the investigation of a new phenomenon—the inertial forces outside the static limit and their difference from those inside the static limit. It is necessary to take into account the relativistic corrections when

one considers the movement of the spacecrafts in this region. This can be achieved by using the rotating frame and observing the signals from the Earth.

In this paper Latin indices take values 0, 1, 2, 3 and Greek indices take values 1, 2, 3.

Inside the static limit

In this paper we consider the flat Minkowski spacetime in cylindrical coordinates {ct, r, ϕ′, z}:

$$ds^2 = c^2dt^2 - dr^2 - r^2d\varphi'^2 - dz^2 \ . \tag{1}$$

If we consider the rotating coordinates in the Minkowski spacetime

$$\varphi' = \varphi - \omega t \ , \tag{2}$$

then we obtain the following line element:

$$ds^2 = c^2dt^2 - r^2(d\varphi - \omega dt)^2 - dr^2 - dz^2 \ . \tag{3}$$

Here ω is angular velocity.

One can note that the metric component g_{00} changes its sign at $r = r_{sl} = \frac{c}{\omega}$. However, the line element (3) might still be timelike due to the positivity of the off-diagonal term $g_{02}dtd\phi = \omega r^2 dtd\phi$. If we compare the metric (3) with the Kerr metric, then the hypersurface $r = r_{sl}$ plays a role of the static limit in the Kerr black hole.

The Killing vector outside the static limit has a different form than inside the static limit i. e. $\frac{d}{dt} + \omega\frac{d}{d\varphi}$. Due to this fact, we have another expression for the proper time where the off-diagonal term is not equal to zero. Thus, the proper time will be imaginary for a body at rest. In this region and the geodesic equations will lead to new phenomenon—the inertial forces.

If we consider the observer on the Earth (motionless with everything rotating around it), then the object which is situated at $r > r_{sl}$ cannot be static for the observer. It must also rotate otherwise the line element (3) will be spacelike. Also, in this case the proper time will be imaginary: if we consider the connection between the proper τ and coordinate t times when $r = const.$, $\phi = const.$, $z = const.$, then we obtain:

$$d\tau = \sqrt{g_{00}}dt \ , \tag{4}$$

and we know that $g_{00} < 0$ at $r > r_{sl}$.

So, if we want to calculate inertial forces for the objects inside the static limit using (4), we have to consider only the region $0 \le r \le r_{sl}$. In this region $g_{00} < 0$. From the Newtonian mechanics we know that acceleration is proportional to force. So, to calculate forces one should use the right hand-side of the geodesic equation:

$$\frac{du^i}{d\tau} = -\Gamma^i_{kl}u^k u^l \ , \tag{5}$$

where Γ^i_{kl} is the Christoffel symbol.

One should note that acceleration is the time derivative of the 4-velocity u^i. From differential geometry we know that the derivative does not obey the tensor transformation law. So, when we define force we should use the covariant derivative instead of the usual one. We want to calculate the three-force, which requires the three covariant derivative instead of (5). Thus, we get (Landau, Lifshitz 1980):

$$f^\alpha = u^\alpha_{;\beta}u^\beta = \frac{du^\alpha}{d\tau} + \gamma^\alpha_{\beta\delta}u^\beta u^\delta \ , \tag{6}$$

where $\gamma^\alpha_{\beta\delta}$ is the purely three-Christoffel symbol. We can note (and show below) that the terms in the right hand-side (5) which are proportional to u^0 correspond to the centrifugal force, while those which

 https://www.doi.org/10.33910/2687-153X-2022-3-3-117-

are proportional to $u^0 u^\alpha$ correspond to the Coriolis force and those which are proportional to $u^\alpha u^\beta$ are part of the three covariant derivative and are not forces at all.

We need the Christoffel symbol of the metric (3) to calculate the geodesic equation (5). Using the well-know formula:

$$\Gamma^i_{kl} = \frac{1}{2} g^{ij} \left(g_{kj,l} + g_{jl,k} - g_{kl,j} \right), \tag{7}$$

one can obtain non-vanishing component of the Christoffel symbols:

$$\begin{aligned} \Gamma^1_{00} &= -\frac{\omega^2 r}{c^2}, \\ \Gamma^1_{02} &= \frac{\omega r}{c}, \\ \Gamma^1_{22} &= -r, \\ \Gamma^2_{12} &= \frac{1}{r}, \\ \Gamma^2_{01} &= -\frac{\omega}{cr}. \end{aligned} \tag{8}$$

To calculate the inertial forces in the region $0 \le r \le r_{sl}$, we can use another well-known formula (Landau, Lifshitz 1980):

$$F_\alpha = \frac{mc^2}{\sqrt{1-\frac{v^2}{c^2}}} \left[-\frac{d}{dx^\alpha} \left(\ln \sqrt{\left(1 - \frac{\omega^2 r^2}{c^2} \right)} \right) + \sqrt{1 - \frac{\omega^2 r^2}{c^2}} \left(\frac{d\xi_\beta}{dx^\alpha} - \frac{d\xi_\alpha}{dx^\beta} \right) \frac{v^\beta}{c} \right], \tag{9}$$

where

$$\begin{aligned} \xi_\alpha &= \frac{g_{0\alpha}}{1 - \frac{\omega^2 r^2}{c^2}}, \\ v^\alpha &= \frac{c dx^\alpha}{\sqrt{1 - \frac{\omega^2 r^2}{c^2}} \left(cdt - \xi_\beta dx^\beta \right)}. \end{aligned} \tag{10}$$

Note that the first term in the square brackets corresponds to the centrifugal force and the second term depends on the velocity linearly and corresponds to the Coriolis force.

Substituting (10) into (9) we obtain:

$$F_r = \left[\frac{mc^2}{\sqrt{1 - \frac{v^2}{c^2}}} \left(\frac{2\omega^2 r}{c^2 - \omega^2 r^2} \right) \right]_{centr} + \left[\frac{2\omega r}{\left(1 - \frac{\omega^2 r^2}{c^2} \right)^2} \frac{d\varphi}{cdt - \xi_2 d\varphi} \right]_{cor}, \tag{11}$$

$$F_\varphi = \left[\frac{2\omega r}{\left(1 - \frac{\omega^2 r^2}{c^2} \right)^2} \frac{dr}{cdt - \xi_2 d\varphi} \right]_{cor}. \tag{12}$$

Let us find out where the static limit r_{sl} is situated in the Solar system. For this purpose let us consider two cases:

1. The static observer is on the surface of the Earth and everything is rotating around it. In this case we should solve the following algebraic equation:

$$1-\frac{\omega^2 r^2}{c^2}=g_{00}=0\ . \tag{13}$$

The period is equal to 24 h and the static limit is situated between the Uranus and the Neptune.

2. Everything is rotating around the Sun and the observer is on the Earth. In this case the period is equal to 1 year and $r_{sl}=1.5\times10^{15}m$. This static limit is situated inside the Oort's clouds.

General case

Here and in what follows we consider the system in units c = 1.

In the general case the proper time τ has the following form:

$$d\tau^2=\left(1-\omega^2r^2\right)dt^2+2\omega r^2dtd\varphi-dr^2-dz^2-r^2d\varphi^2\ . \tag{14}$$

One can see that the square of proper time (14) might be positive in the region $r_{sl}=\frac{1}{\omega}<r<+\infty$ because of the off-diagonal term $+2\omega r^2dtd\varphi$. Hence we state that we can consider the region $r_{sl}<r<+\infty$ only in the case when the observer has non-vanishing angular velocity $\Omega=\frac{d\varphi}{dt}$. However, we assume that $r = const.$ and $r = const.$ for the observer and the connection between the proper and coordinate times is the following:

$$d\tau=dt\sqrt{1-r^2(\Omega-\omega)^2}\ . \tag{15}$$

To obtain force expression we should write down geodesic equations which, in the general case, are given by:

$$\begin{aligned}\frac{d^2r}{d\tau^2}&=\omega^2r\left(\frac{dt}{d\tau}\right)^2-2\omega r\frac{dt}{d\tau}\frac{d\varphi}{d\tau}+r\left(\frac{d\varphi}{d\tau}\right)^2\ ,\\ \frac{d^2\varphi}{d\tau^2}&=-\frac{2}{r}\frac{dr}{d\tau}\frac{d\varphi}{d\tau}+2\frac{\omega}{r}\frac{dt}{d\tau}\frac{dr}{d\tau}\ ,\end{aligned} \tag{16}$$

If we followed the definition of force from the previous section, then we would see that forces have finite values on the static limit but they are extremely large. No one sees these large values so we should redefine forces.

In the previous section we defined forces as three covariant derivative of the momentum and did not count some terms in the right-hand side of the equation (16) because they were part of the three covariant derivative. However, in the general case, outside the static limit, the Killing vector $\frac{d}{dt}$ is spacelike and as the result is unphysical. In the region $r > r_{sl}$ the observer, like in the ergoregion of a rotating black hole, has to move along both t and ϕ coordinates. As the result of such movement all the Christoffel symbols proportiaonal to $(u^0)^2$, u^0u^φ and $(u^\varphi)^2$ are inertial forces. So substituting (15) into (16) one obtains:

$$\begin{aligned}\frac{d^2r}{d\tau^2}&=\frac{r}{1-r^2(\omega-\Omega)^2}\left(\Omega-\omega\right)^2\ ,\\ \frac{d^2\varphi}{d\tau^2}&=\frac{2v_r}{r-r^3(\omega-\Omega)^2}\left(\omega-\Omega\right)\ ,\\ v_r&=\frac{dr}{dt}\ .\end{aligned} \tag{17}$$

From (17) one can see that the object has non-vanishing acceleration only if $\omega-\Omega\neq0$. The object does not have any acceleration if $\Omega=\omega$ because in this case it is equal to zero. If $\omega\neq\Omega$, then the acceleration is a growing function of r and $r=\frac{1}{\omega-\Omega}$ diverges at the surface. This situation is the same like in the

 https://www.doi.org/10.33910/2687-153X-2022-3-3-117-

previous section with the angular velocity ω being replaced by $\omega - \Omega$. If the acceleration of an object is a constant W, then the $\Omega = \frac{d\varphi}{dt}$ is the decreasing function of r, i. e.:

$$\Omega = \omega - \sqrt{\frac{W}{r + Wr^2}} \ . \tag{18}$$

As is seen, with the proper time (15) we should redefine inertial forces. It leads us to the fact that if $\Omega = \omega$, then the acceleration is absent. However, if the body has constant acceleration, it means that $\Omega \neq \omega$ but $\omega - \Omega$ tends to zero with growing r. Also, one should notice that Ω must always be positive otherwise all metric components become negative outside the static limit and the line element (16) would be spacelike in this region. However, in the region $0 \leq r \leq r_{sl}$ we can consider negative values of ω.

Conclusion

In this paper we have considered forces inside and outside the static limit in the Minkowski spacetime for rotating coordinates. This frame has only two types of inertial forces, i. e., centrifugal and the Coriolis forces. In the case of the static bodies one can consider forces only up to the radius $r = r_{sl}$ because in this case the proper time and velocity is imaginary outside the static limit. Thus, to consider the inertial forces in the region $r_{sl} \leq r \leq \infty$ one should consider the general proper time with non-vanishing angular velocity $\Omega = \frac{d\varphi}{dt}$. We have found out that with the proper time (15), the acceleration tends to zero if $\Omega \to \omega$. It should be also noted that if $\omega \neq \Omega$, then we have another surface $r = \frac{1}{\omega - \Omega}$. This surface shows that the line element outside it (3) is spacelike. That is, the case $\omega \neq \Omega$ is an analogue of the static observer with the angular momentum of spacetime $\omega - \Omega$. It is worth mentioning that all forces which are considered in this article are fictitious ones.

Conflict of Interest

The authors declare that there is no conflict of interest, either existing or potential.

Author Contributions

The authors have made an equal contribution to the preparation of the text.

References

Grib, A. A., Pavlov, Y. V. (2011) Particles with negative energies in black holes. *International Journal of Modern Physics D*, 20 (05), 675–684. https://doi.org/10.1142/S0218271811019013 (In English)

Grib, A. A., Pavlov, Y. V., Vertogradov, V. D. (2014) Geodesics with negative energy in the ergosphere of rotating black holes. *Modern Physics Letters A*, 29 (20), article 1450110. https://doi.org/10.1142/S0217732314501107 (In English)

Grib, A. A., Pavlov, Yu. V. (2019) Static limit and Penrose effect in rotating reference frames. *Theoretical and Mathematical Physics*, 200 (2), 1117–1125. https://doi.org/10.1134/S004057791908004X (In English)

Landau, L. D., Lifshitz, E. M. (1980) *Course of theoretical physics series. Vol. 2. The classical theory of fields*. 4th ed. Oxford: Butterworth-Heinemann Publ., 444 p. (In English)

Vertogradov, V. D. (2015) Geodesics for particles with negative energy in Kerr's metric. *Gravitation and Cosmology*, 21 (2), 171–174. https://doi.org/10.1134/S0202289315020115 (In English)

Theoretical physics.
Theory of condensed matter

UDC 538.9

EDN QAMJZS
https://www.doi.org/10.33910/2687-153X-2022-3-3-122-136

Numerical simulations of nonlinear and chaotic order parameter responses in bulk antiferroelectrics using ammonium dihydrogen phosphate parameter

S.-Ch. Lim✉[1]

[1] Universiti Sains Malaysia, 11800 USM Penang, Malaysia

Authors

Lim Siew-Choo, ORCID: 0000-0001-8397-0886, e-mail: sclim@usm.my

For citation: Lim, S.-Ch. (2022) Numerical simulations of nonlinear and chaotic order parameter responses in bulk antiferroelectrics using ammonium dihydrogen phosphate parameter. *Physics of Complex Systems*, 3 (3), 122–136. https://www.doi.org/10.33910/2687-153X-2022-3-3-122-136 EDN QAMJZS

Received 22 April 2022; reviewed 9 June 2022; accepted 9 June 2022.

Funding: The study did not receive any external funding.

Abstract. In this paper, the nonlinear and chaotic responses of bulk antiferroelectrics are elaborated phenomenologically and numerically. The first ordered phase of bulk antiferroelectrics is formulated by applying calculus of variations to Landau free energy density expansions of bulk antiferroelectrics. With applied time-dependent electric field, the antiferroelectrics dynamic responses are obtained by Landau–Khalatnikov equation of motion. The resulting dynamical equations are two nonlinearly-coupled second order differential equations corresponding to two inter-penetrating sub-lattices of antiferroelectrics, and these are solved numerically using forth-order Runge–Kutta methods and ammonium dihydrogen phosphate parameters in its first ordered phase. These calculated results are presented graphically for various frequencies and amplitudes in the applied electric fields.

Keywords: antiferroelectrics, ammonium dihydrogen phosphate, chaos, Landau free energy density, nonlinear, Poincare Sections

Introduction

Some switching processes and nonlinear chaotic dynamics in second order ferro- and anti-ferromagnetic systems have been studied theoretically using Landau–Lifshitz equations of motion (Chan 2010; Toh 2009). For ferroelectric system, i. e., triglycine sulfate, the similar studies have been carried out theoretically and numerically using Landau theory, and experimentally by measuring responses of ferroelectric capacitor in series resonance circuit (Diestelhorst 2003). The switching processes and some conventional nonlinear responses in ferro- and anti-ferroelectrics have been discussed and studied (Lines, Glass 1977; Tan 2001). However, the nonlinear chaotic behaviors of antiferroelectrics are still left behind. It is of interest to study nonlinear chaotic dynamics in antiferroelectric systems. The context of this paper is focused on theoretical and numerical studies of chaotic dynamics in bulk antiferroelectric system in its first ordered phase. In the numerical simulations, the fourth-order Runge–Kutta method is adopted (Press et al. 1996, 704; Strogatz 2018, 33), and is based on the parameters of ammonium dihydrogen phosphate (ADP) at 80 *K* (Ledzion et al. 2004). These numerical results are presented graphically.

Formalism

The formalism in this section is adopted and generalized from the Landau theory of first order ferroelectrics (FE) and second order antiferroelectrics (AFE) explained in Lines and Glass (1977). In general, the bulk AFE thermodynamic potential, G, is

$$G = U - TS - X_j x_j - E_i D_i \tag{1}$$

where subscript i represents all the existing field components in the AFE system. U is the internal energy of the system, T is the temperature, S is the entropy, X_j is the thermal stress, x_j is the strain, E_i is the electric field induced by the system's spontaneous polarizations and the applied electric field, and D_i is the electric displacement.

For the study of AFE, it is convenient to describe the system as two interpenetrating sublattices, namely sublattice-A and sublattice-B. Let D_A and D_B represent electric displacements, and E_A and E_B represent electric fields for sublattice-A and -B, respectively. With the assumptions that the system has zero stress and strain, the volume and temperature of the system remains constant in the applied electric field, the thermodynamic potential is isobaric and isothermal, Equation (1) can be rewritten as a polynomial of order parameters of sublattices, i.e., displacements of the two sublattices, D_A and D_B:

$$G = \alpha_1\left(D_A^2 + D_B^2\right) - 2\alpha_{11}\left(D_A^4 + D_B^4\right) + \alpha_{111}\left(D_A^6 + D_B^6\right) + \eta D_A D_B - E_A D_A - E_B D_B \tag{2}$$

where α_1, α_{11}, and α_{111} are constants, referred to as Landau coefficients, and η is the interaction constant of the two sublattices. For AFE, η has positive value, which facilitates an antipolar situation. The negative signs of the fourth order terms represent a first order transition of the AFE system, and the constant 2 in front of α_{11} is for the convenience of the following derivations. In order to enable the fitting of experimental measurements, additional pairs of variables, i. e., staggered displacement $R = D_A - D_B$, staggered field $E_S = E_A - E_B$, normal displacement $Q = D_A + D_B$, and the Maxwell field $E_M = E_A + E_B$ are defined (Lines, Glass 1977, 88). In terms of Q, R, E_M, and E_S, Equation (2) becomes

$$\begin{aligned} G = &\left(\frac{\alpha_1}{2} + \frac{\eta}{4}\right)Q^2 + \left(\frac{\alpha_1}{2} - \frac{\eta}{4}\right)R^2 - \frac{\alpha_{11}}{4}\left(Q^4 + 6Q^2R^2 + R^4\right) + \\ &+ \frac{\alpha_{111}}{32}\left(Q^6 + 15Q^4R^2 + 15Q^2R^4 + R^6\right) - \frac{1}{2}E_M Q - \frac{1}{2}E_S R \end{aligned} \tag{3}$$

For antiferroelectrics, the staggered field is necessarily zero, i. e., $E_S = 0$. α_1 is temperature dependent, and is defined as $\alpha_1 = \frac{\eta}{2} + \beta\left(T - T_C\right)$. Then, Equation (3) becomes

$$\begin{aligned} G = &\frac{1}{2}\left[\eta + \beta\left(T - T_C\right)\right]Q^2 + \frac{1}{2}\beta\left(T - T_C\right)R^2 - \frac{\alpha_{11}}{4}\left(Q^4 + 6Q^2R^2 + R^4\right) + \\ &+ \frac{\alpha_{111}}{32}\left(Q^6 + 15Q^4R^2 + 15Q^2R^4 + R^6\right) - \frac{1}{2}E_M Q \end{aligned} \tag{4}$$

where β is a constant, and T_C is the Curie temperature of the AFE system.

In order to ease the numerical simulations, reduced variables, or dimensionless quantities, we introduced g_A, t, e, q, r, and ψ, corresponding to thermodynamic potential of AFE system, G, temperature, T, applied Maxwell field, E_M, normal displacement, Q, and staggered displacement, R, and interaction constant of sublattices, η, as defined in Equations (5):

$$G = \frac{16\alpha_{11}^3}{\alpha_{111}^2} g_A \tag{5a}$$

$$\beta\left(T-T_C\right)=\frac{4\alpha_{11}^2}{\alpha_{111}}t \tag{5b}$$

$$E_M=8\sqrt{\frac{\alpha_{11}^5}{2\alpha_{111}^3}}e \tag{5c}$$

$$Q=\sqrt{\frac{8\alpha_{11}}{\alpha_{111}}}q \tag{5d}$$

$$R=\sqrt{\frac{8\alpha_{11}}{\alpha_{111}}}r \tag{5e}$$

$$\eta=\frac{4\alpha_{11}^2}{\alpha_{111}}\psi \tag{5f}$$

The substitution of Equations (5) in Equation (4) results in dimensionless thermodynamic potential:

$$g_A=\left(\psi+t\right)q^2+tr^2-\left(q^4+6q^2r^2+r^4\right)+\left(q^6+15q^4r^2+15q^2r^4+r^6\right)-eq. \tag{6}$$

Equation (6) is used in the formalism of nonlinear dynamical equations in the following sections.

ψ and t values are fitted by using material parameters of ammonium dihydrogen phosphate (ADP), an order-disorder AFE, which always shatter at the transition temperature. The Curie–Weiss law, i. e., $\varepsilon=\varepsilon_\infty+\frac{C_1}{T-T_1}$, is used to fit the value of ψ, where ε_∞, C_1 and T_1 are high frequency limit dielectric constant, the Curie constant and the Curie–Weiss temperature, respectively (Ledzion et al. 2004). The assumptions here are that the value of ψ is constant with respect to varying temperature and applied electric field.

For ADP, the Curie constant, the Curie–Weiss temperature and the Curie temperature are C_1 = 10160 K, T_1 = 22.7 *K*, and T_C = *148 K*, respectively (Ledzion et al. 2004; Milek, Neuberger 1972, 44). Below the Curie temperature, the fitting of ADP material constants with the Curie–Weiss law gives spontaneous sublattice polarization, $P_0\approx 0.081\ C\times m^{-2}$ and $\psi\approx 0.01233$ (the corresponding $\eta\approx 1.393\times 10^9$). At T = 80*K* ($t\approx -3.346\times 10^{-3}$), one unit of e is approximately equivalent to $1.1206\times 10^{10}\ V\cdot m^{-1}$, and one unit of q is approximately equivalent to $0.1984\ C\times m^{-2}$.

Derivations of nonlinear dynamical equations

With the presence of time dependent electric field, the Lorentz force per unit volume exerting on the AFE system is given by $\varphi\frac{\partial G}{\partial\overline{D_i}}$, and the resulting Landau–Khalatnikov equation of motion from Newton's Second law is

$$\bar{m}\frac{d^2\overline{D_i}}{d\tau^2}+\bar{\gamma}\frac{d\overline{D_i}}{d\tau}=-\varphi\frac{\delta G}{\delta\overline{D_i}} \tag{7}$$

The first and second terms in Equation (7) represent acceleration and damping of the charge motion. $\frac{\delta G}{\delta\overline{D_i}}$ is the variation of AFE free energy density, G in Equation (4), with respect to quantity $\overline{D_i}$, in which $\overline{D_i}$ represents the Maxwell and staggered displacements, i. e., Q and R. ϕ is the sublattice charge

 https://www.doi.org/10.33910/2687-153X-2022-3-3-122-136

density, $\overline{m}$ is the mass per unit charge, and $\overline{\gamma}$ is the mass per unit charge per second of the AFE system. For small damping, the dynamics of the Maxwell and staggered displacements are oscillatory.

In terms of dimensionless time variable *s*, and dimensionless damping constant *g*, defined as $\tau = \sqrt{\frac{m\alpha_{111}}{2\alpha_{11}^2}}\, s$, $\gamma = \sqrt{\frac{2m\alpha_{11}^2}{\alpha_{111}}}\, g$ where $m = \overline{m} / \varphi$ and $\gamma = \overline{\gamma} / \varphi$, and the previous dimensionless variables *t, e, q, r,* and ψ, the dimensionless oscillatory equations of motion are:

$$\frac{d^2q}{ds^2} + g\frac{dq}{ds} = -2(\psi + t)q + 4\left(q^3 + 3qr^2\right) - 6\left(q^5 + 10q^3r^2 + 5qr^4\right) + e \tag{8a}$$

$$\frac{d^2r}{ds^2} + g\frac{dr}{ds} = -2tr + 4\left(3q^2r + r^3\right) - 6\left(5q^4r + 10q^2r^3 + r^5\right) \tag{8b}$$

Compare with the Duffing oscillator equations of motion (Goldstone, Garmire 1984), Equations (8) are more complicated with extra fifth order terms on the right side of the equations. Because of the existence of third and fifth order nonlinear terms, Equations (8) can be solved only numerically. These coupled equations are used to numerically simulate nonlinear and chaotic dynamics in the AFE system. In the numerical simulations, the fourth-order Runge–Kutta method is adopted (Press et al. 1996, 704; Strogatz 2018, 33), and is based on AFE material parameters and constants. The chosen antiferroelectric material is Ammonium Dihydrogen Phosphate (ADP) at temperature $T = 80\ K$. For ADP, the dimensionless interaction constant between AFE sublattices and temperature are $\psi \approx 0.0123$ and $t \approx -3.346 \times 10^{-3}$, and dimensionless critical field is $e_C \approx 0.4166$ (corresponding to critical applied electric to switch ADP from antiferroelectric to paraelectric states, i. e., $E_C \approx 4.668 \times 10^9$ V × m^{-1}). The scaled natural frequency, ω_0, of ADP is obtained from Equation (10a) by dropping all the dissipating and nonlinear terms. For ADP, $\omega_0 \approx \sqrt{2(\psi + t)} \approx 0.1341$ per unit *s* (dimensionless time). This shows that the natural frequency is temperature dependent (Ledzion, Bondarczuk, Kucharczyk 2004).

Nonlinear and chaotic states of AFE from numerical simulations

The numerical simulations are carried out by applying the dimensionless time varying sinusoidal Maxwell field, *e* (corresponding to E_M), to Equations (8). It is represented by $e = e_0 \sin(\omega s)$. As an example, this field is shown in Figure 1 for $\omega = 1.0\ \omega_0$, and $e_0 = 0.6\ e_C$.

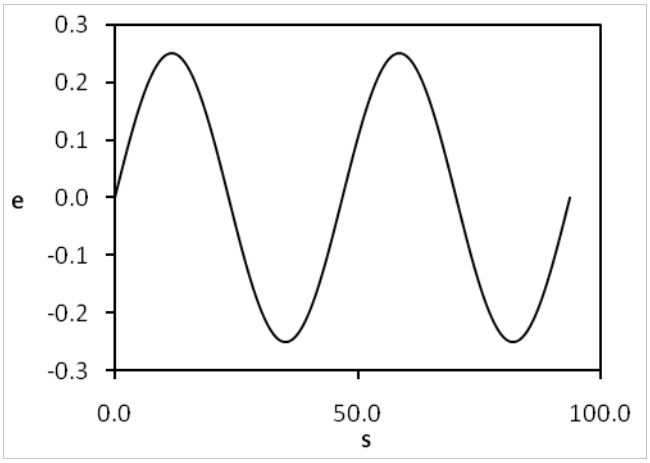

Fig. 1. *e* versus *s* with $\omega = 1.0\ \omega_0$, and $e_0 = 0.6\ e_C$

The calculations are started with extremely low frequency and extremely small amplitude of *e*, i. e., $\omega = 4.0 \times 10^{-3}\ \omega_0$ and $e_0 = 1.0 \times 10^{-13}\ e_C$. These values are close to the lowest limits computable by the numerical programming. The values of ω and e_0 are increases in the subsequent calculations to exhibit their effects on the AFE system. The value of damping is the same for all simulations, i. e., the value for reduced damping is $g = 0.01$. The numerical results for each applied field are plotted in four figures, (a) shows the reduced/dimensionless normal displacement, *q*, versus reduced time, *s*, (b) shows the reduced normal displacement, *q*, versus the reduced applied Maxwell field, *e*, (c) shows the phase diagram of the system, i. e.,

time derivative of reduced normal displacement, *dq/ds*, versus reduced normal displacement, *q*, and, (d) shows the Poincare Sections of the phase diagram started on 1/8 cycle for 200 cycles. The duration for numerical results in (a) to (c) are two cycles, as in Figure 1.

The numerical results for $e_0 = 1.0 \times 10^{-13}\ e_C$ and $\omega = 4.0 \times 10^{-3}\ \omega_0$, are shown in Figures 2(a) to 2(d). At this small applied field amplitude and low frequency, the AFE system exhibits linear response to *e*, with the *q* versus *s* curve in Figure 2(a) is exactly the same pattern as the curve *e* versus *s* in Figure 1. This linearity is further affirmed in Figure 2(b), the curve of AFE state is a straight line through the origin of the *q* versus *e* axes. The phase diagram of the system is plotted in Figure 2(c). The elliptical closed curve shows that the attractor for the AFE system is at the origin of the amplitude of applied field and value of frequency. The regularity and periodicity in dynamical response of this AFE system under driven applied field are shown by the Poincare Sections plotted in Figure 2(d), in which 200 points are taken with 2π phase increases for each subsequent point, started from 1/8 cycle. Figure 2(d) shows almost an overlapping of these points.

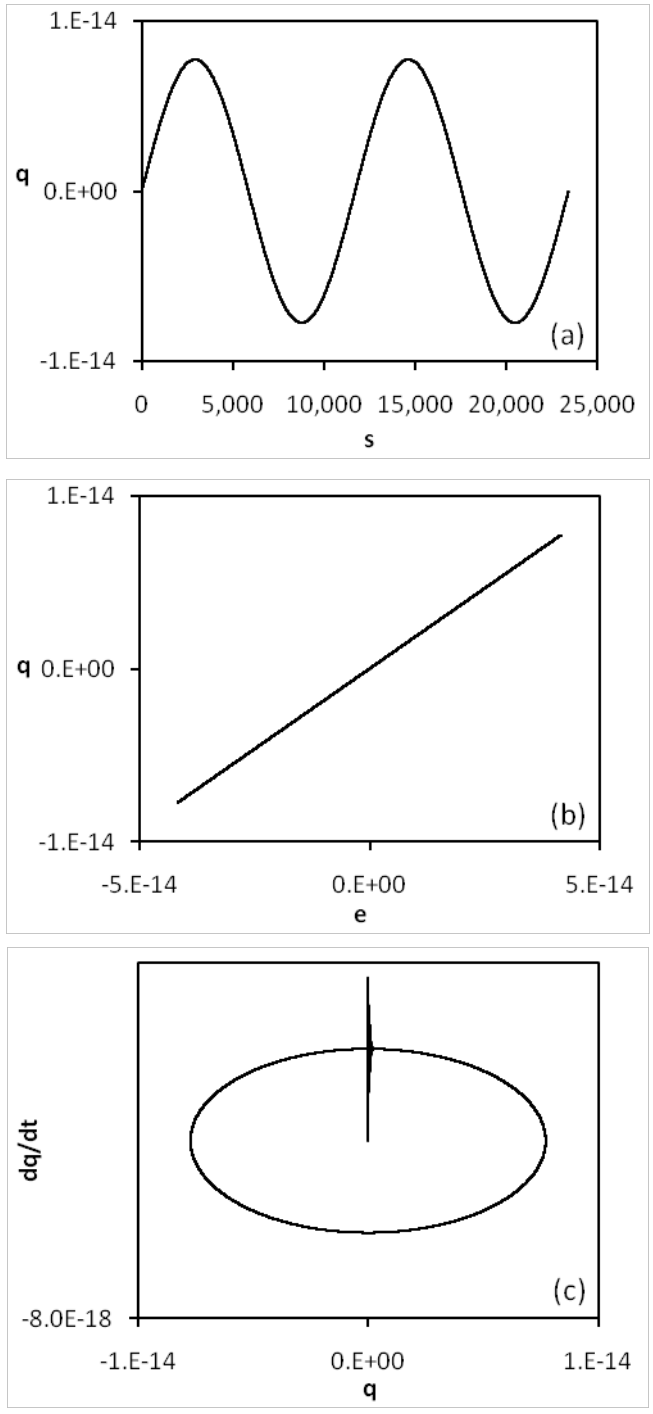

Fig. 2. AFE's phase diagrams when $\omega = 4.0 \times 10^{-3}\ \omega_0$, and $e_0 = 1.0 \times 10^{-13}\ e_C$

https://www.doi.org/10.33910/2687-153X-2022-3-3-122-136

For applied field amplitude and frequency increased to $e_0 = 1.0 \times 10^{-5}\, e_C$ and $\omega = 0.1\, \omega_0$, the numerical results are shown in Figures 3(a) to 3(d). At these values of applied field amplitude and frequency, the AFE system exhibits period multiplication centered on sinusoidal wave as shown in Figures 3(a). This period multiplication is further exhibit in Figure 3(b), with the wavy features centered on the line of AFE state. The corresponding phase diagram of the system is plotted in Figure 3(c). In the phase diagram, the period multiplication exhibits as multiple ellipses skewed to the right. The corresponding Poincare Sections are plotted in Figure 3(d). The Poincare Sections show an overlapping to only four points, this means the responses of the AFE system are quasi-periodic in these small values of applied field amplitude and frequency.

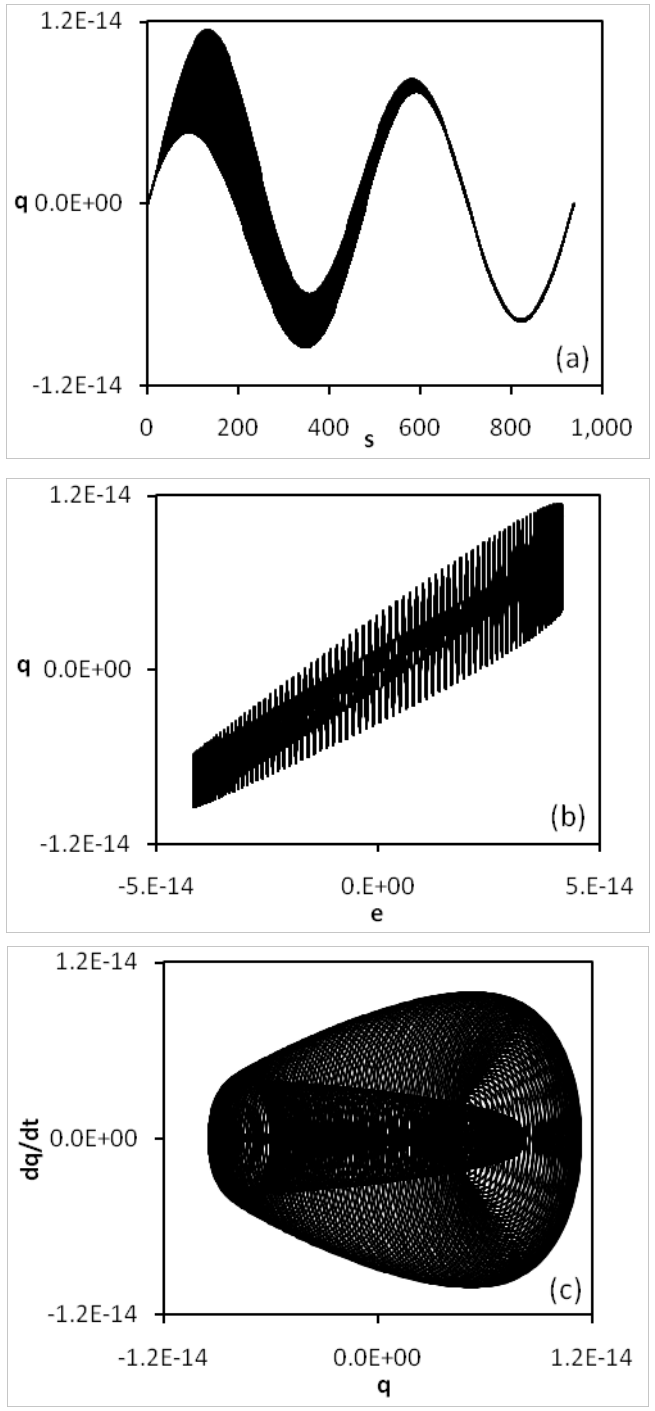

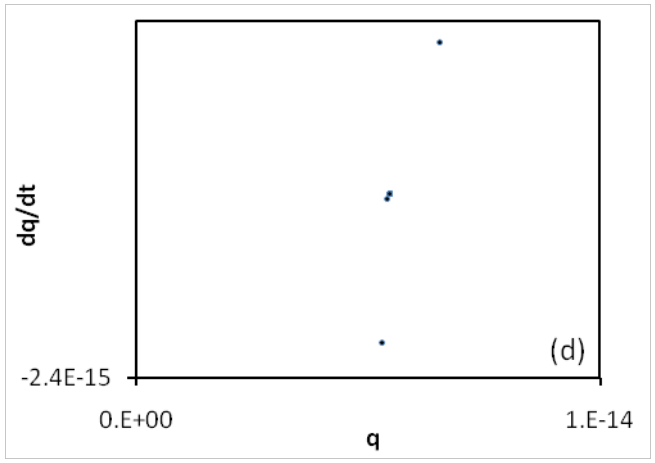

Fig. 3. AFE's phase diagrams when $\omega = 0.1\ \omega_0$, and $e_0 = 1.0 \times 10^{-5}\ e_C$

With applied frequency maintains at $\omega = 0.1\ \omega_0$, the subsequent increases of applied field amplitude to (i) $e_0 = 0.3\ e_C$, (ii) $e_0 = 0.95\ e_C$, (iii) $e_0 = 1.0\ e_C$, (iv) $e_0 = 100.0\ e_C$, and, (v) $e_0 = 2.0 \times 10^6\ e_C$, are plotted in Figures 4 to 8. From the curves and Poincare Sections in Figures 4 to 7, the features of quasi-periodicity decrease as applied field amplitude increases.

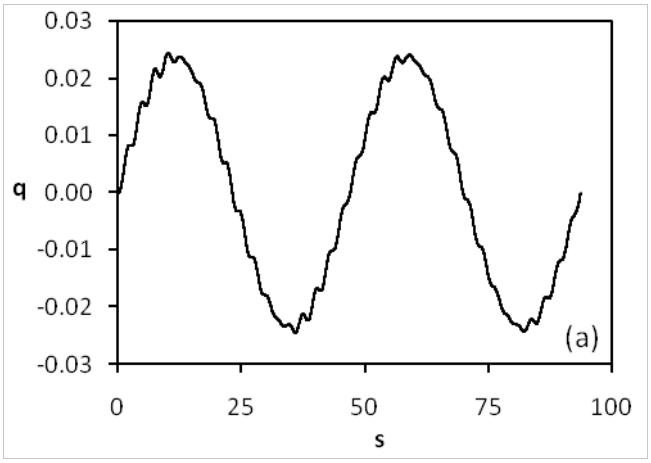

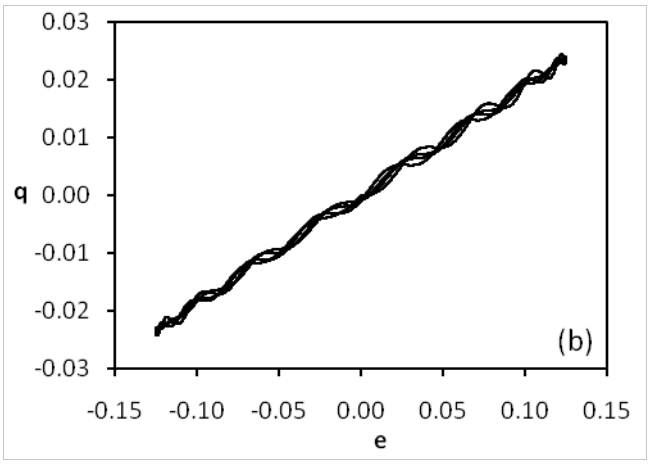

 https://www.doi.org/10.33910/2687-153X-2022-3-3-122-136

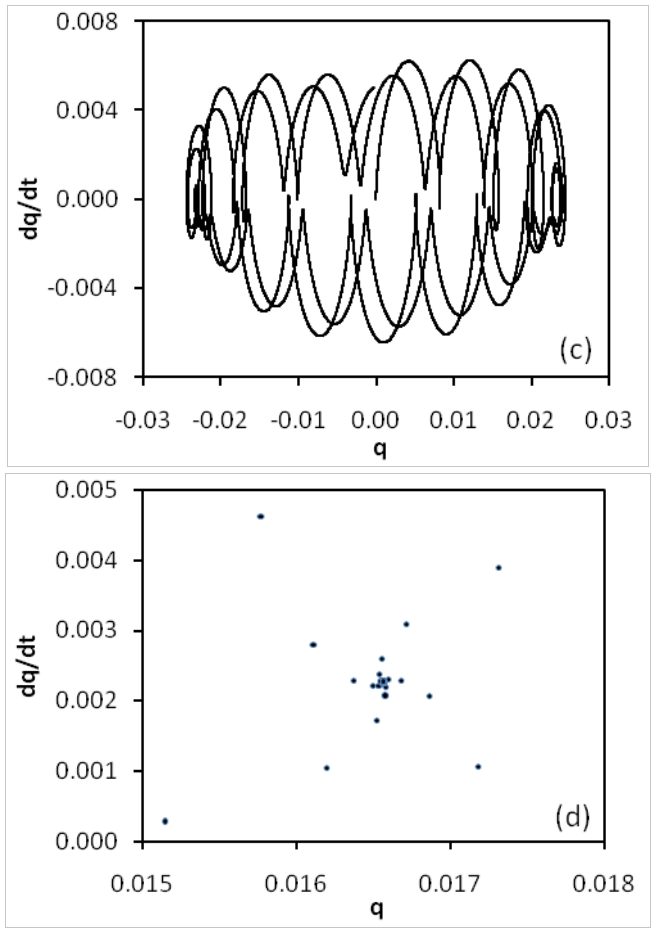

Fig. 4. AFE phase diagrams when $\omega = 1.0\ \omega_0$, and $e_0 = 0.3\ e_C$

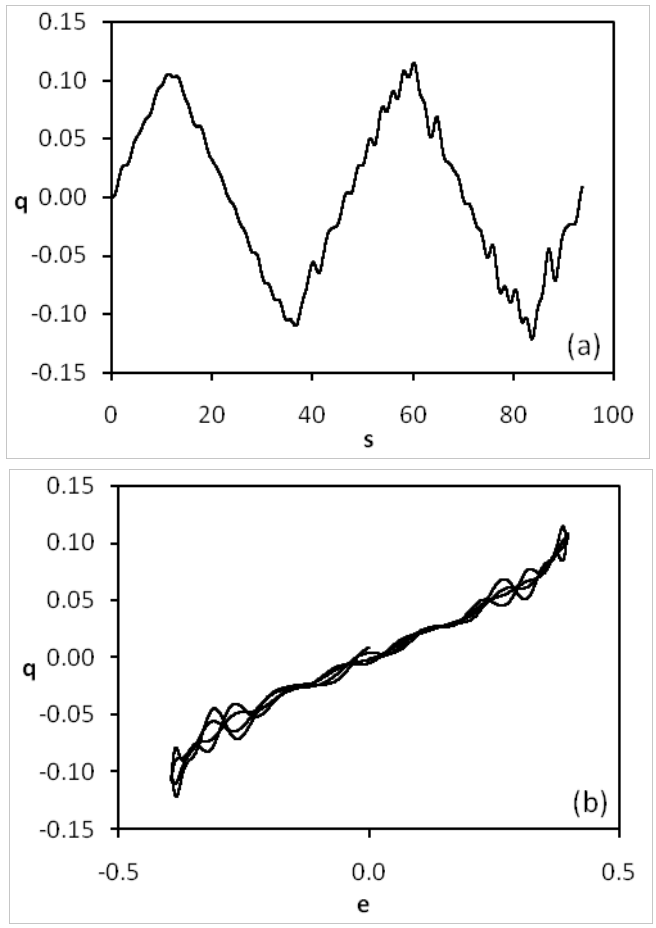

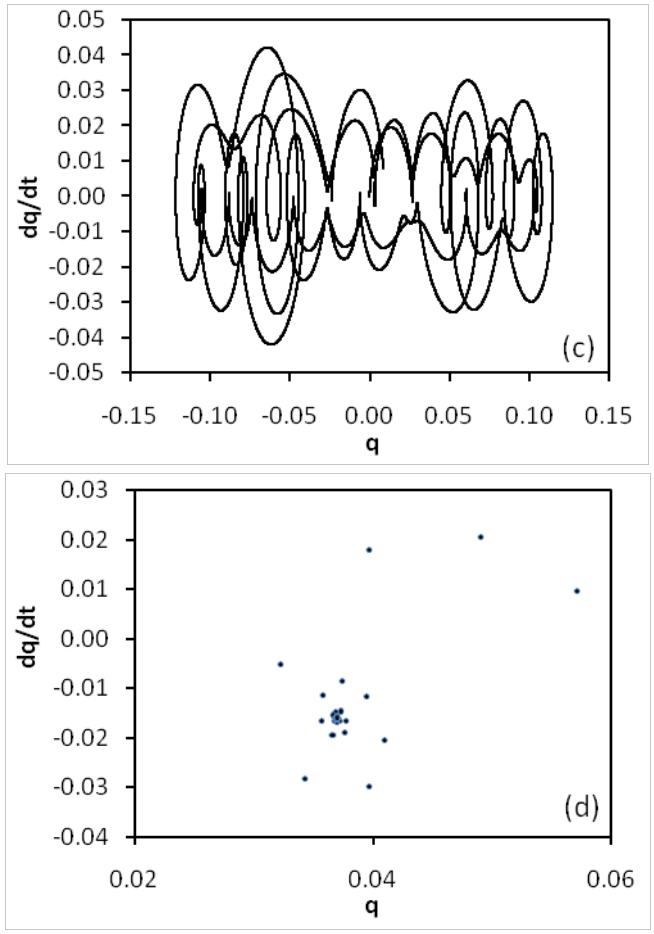

Fig. 5. AFE phase diagrams when $\omega = 1.0\ \omega_0$, and $e_0 = 0.95\ e_C$

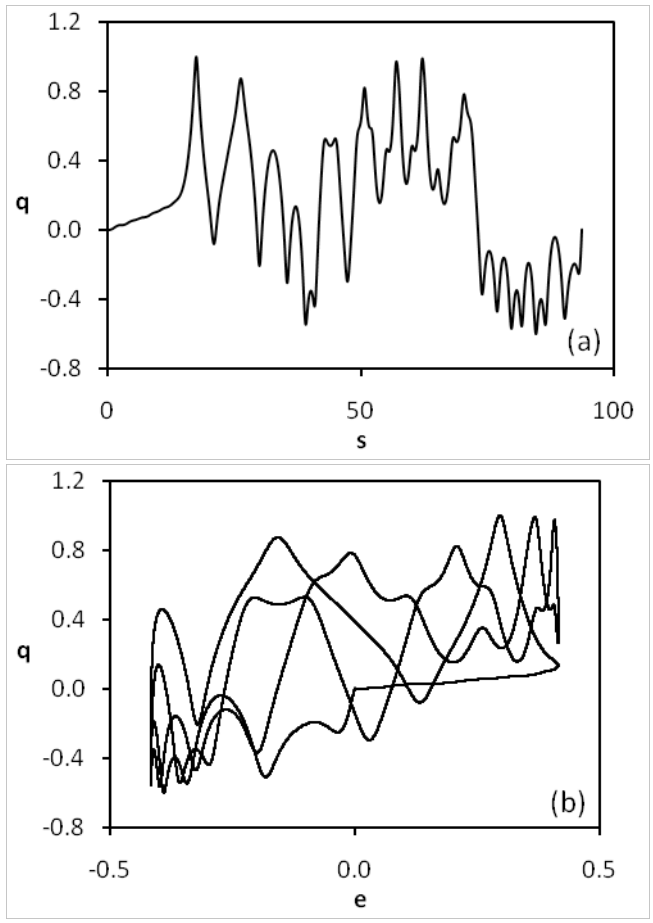

 https://www.doi.org/10.33910/2687-153X-2022-3-3-122-136

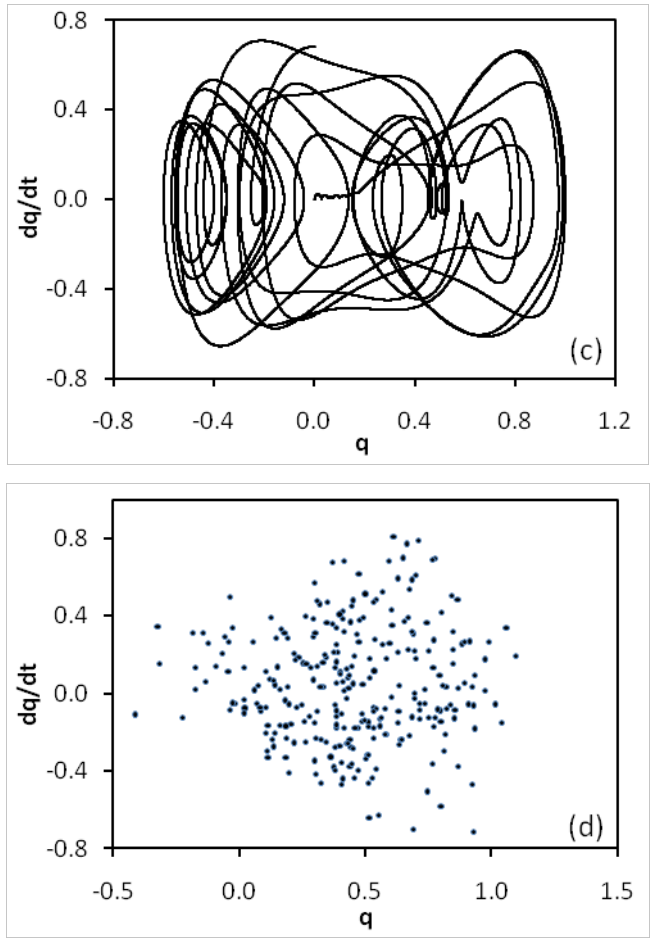

Fig. 6. AFE phase diagrams when $\omega = 1.0\ \omega_0$, and $e_0 = 1.0\ e_C$

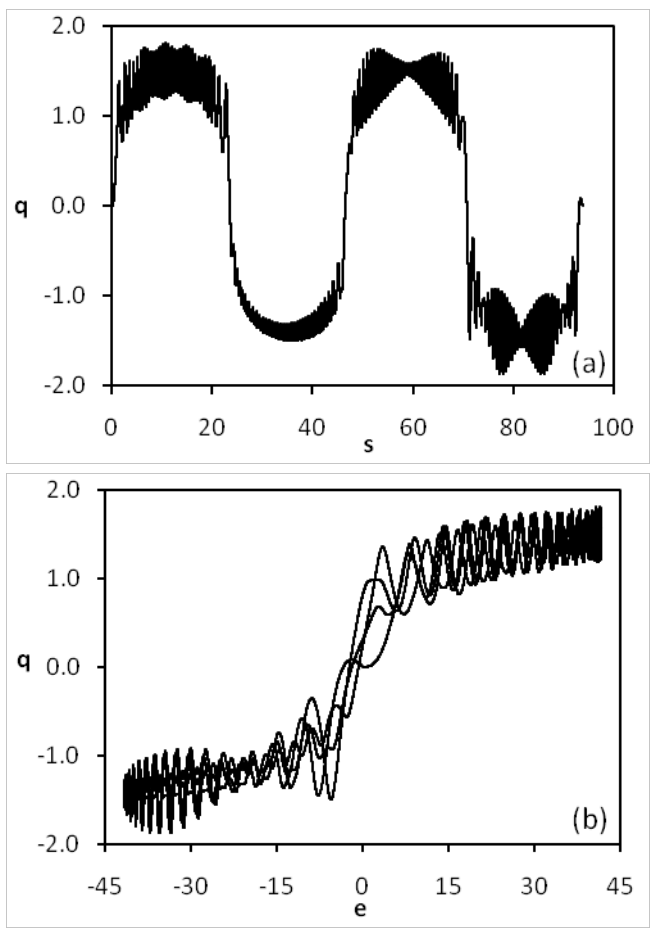

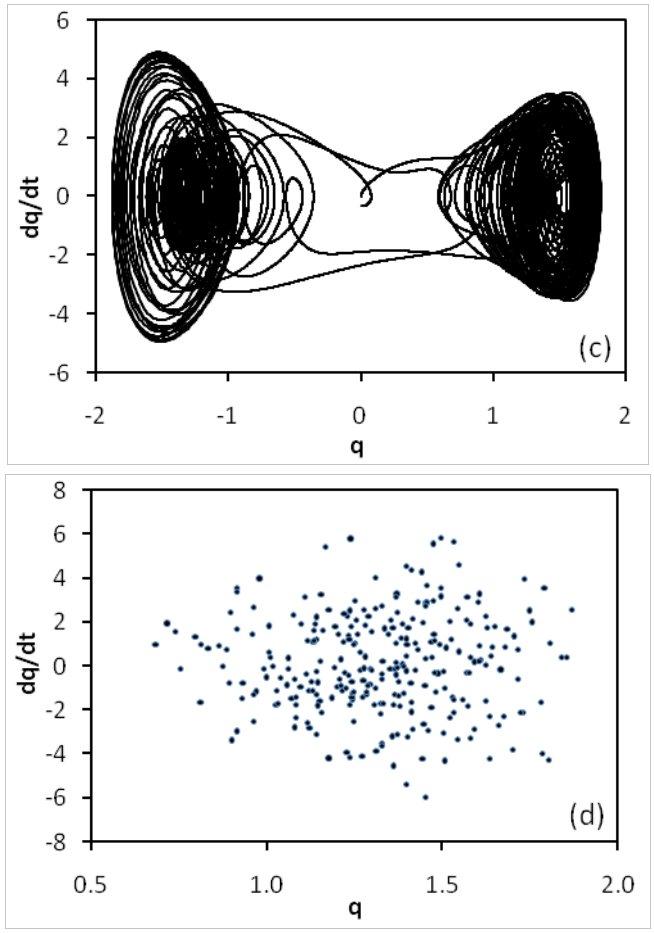

Fig. 7. AFE phase diagrams when $\omega = 1.0\ \omega_0$, and $e_0 = 100.0\ e_C$

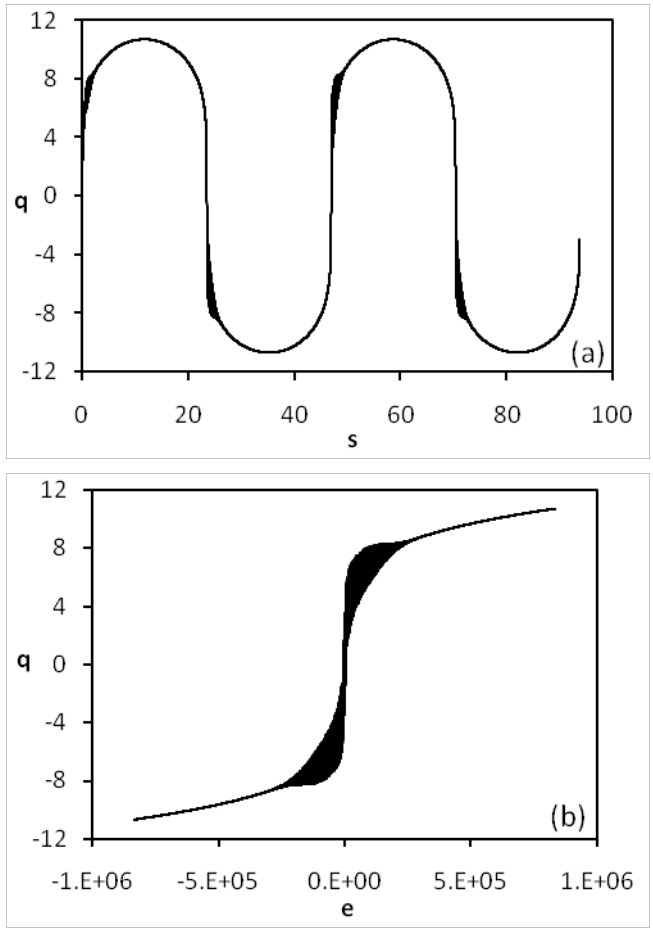

 https://www.doi.org/10.33910/2687-153X-2022-3-3-122-136

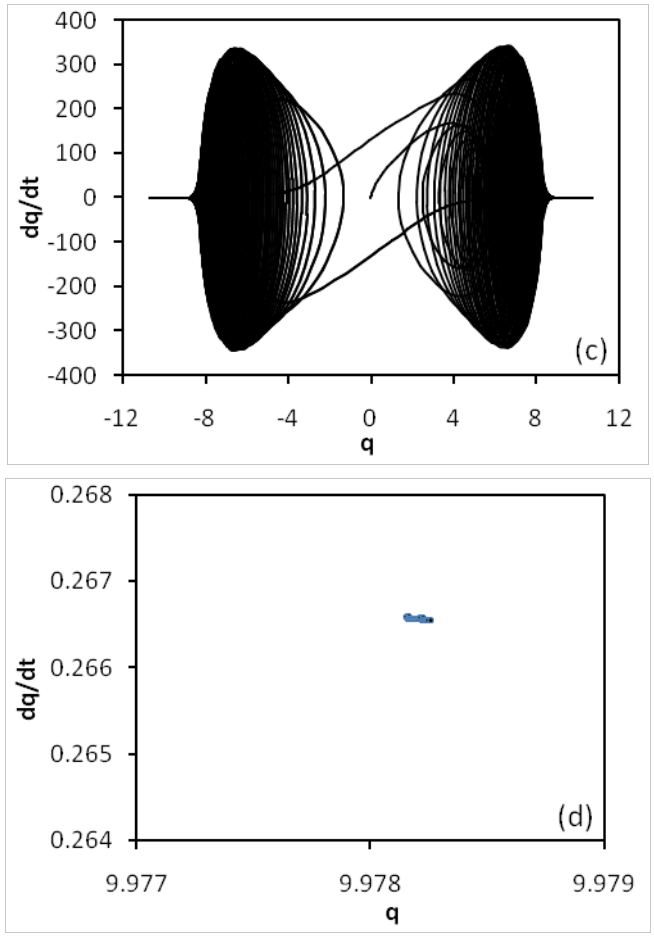

Fig. 8. AFE phase diagrams when $\omega = 1.0\ \omega_0$, and $e_0 = 2.0 \times 10^6\ e_C$

When the applied field amplitude is extremely high as in Figures 8, with $e_0 = 2.0 \times 10^6\ e_C$ close to the upper limit computable by the numerical programming, the q versus s curve in Figure 8(a) is aperiodic, chaotic, and is highly distorted from sinusoidal shape, with little wavelike features in the first and third quadrants of each cycle. These features are more obvious in Figure 8(b). The curve of the AFE state, i. e., q versus e, shows wavelike features in between a double hysteresis loop. The corresponding phase diagram is plotted in Figure 8(c), which is also identified as butterfly curves of the AFE system. In the phase diagram, the curves are winding around two values of q, one is positive, the other one is negative, which are identified as a set of strange attractors (Strogatz 2018). The Poincare Sections in Figure 8(d) show one segment of line, this means the responses of the AFE system in subsequent cycles are very close but not overlapping.

With the applied field amplitude maintained at $e_0 = 0.6\ e_C$, the subsequent increases of applied frequency to (i) $\omega = 2.0\ \omega_0$, and, (ii) $\omega = 3.0\ \omega_0$, are plotted in Figures 9 and 10, respectively. From the curves and Poincare Sections in Figures 9 and 10, the features of quasi-periodicity decrease as applied field frequency increases. This is obvious in the Poincare Sections, as Figure 10(d) shows more branches of points than Figure 9(d).

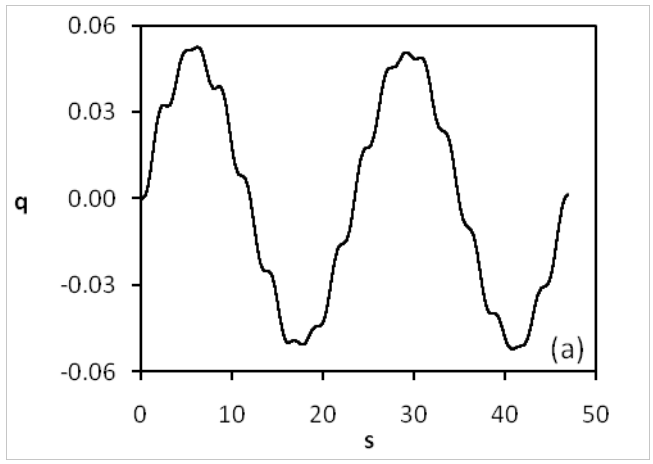

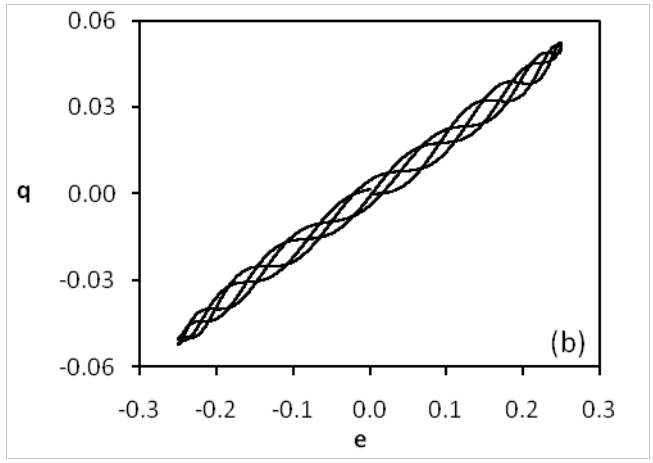

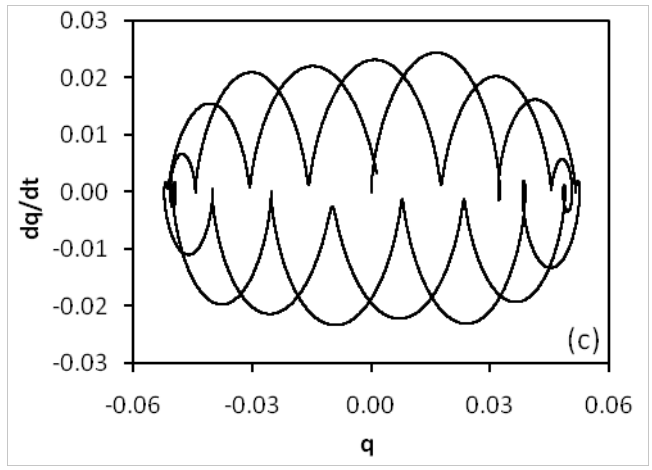

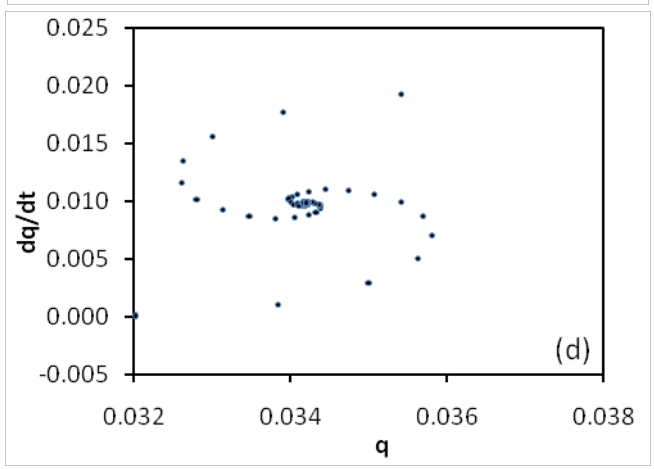

Fig. 9. AFE phase diagrams when $\omega = 2.0\ \omega_0$, and $e_0 = 0.6\ e_C$

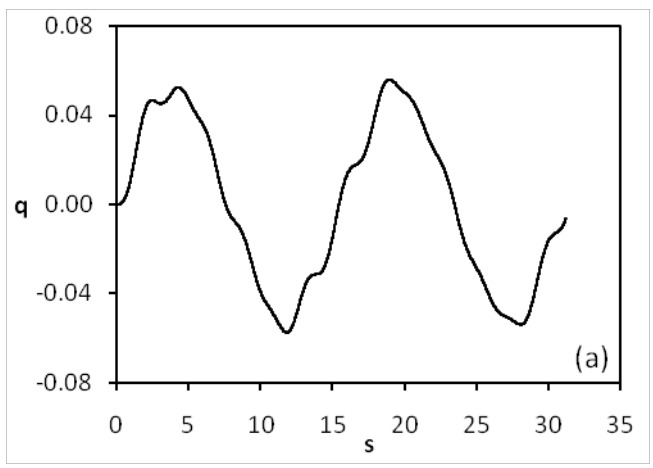

https://www.doi.org/10.33910/2687-153X-2022-3-3-122-136

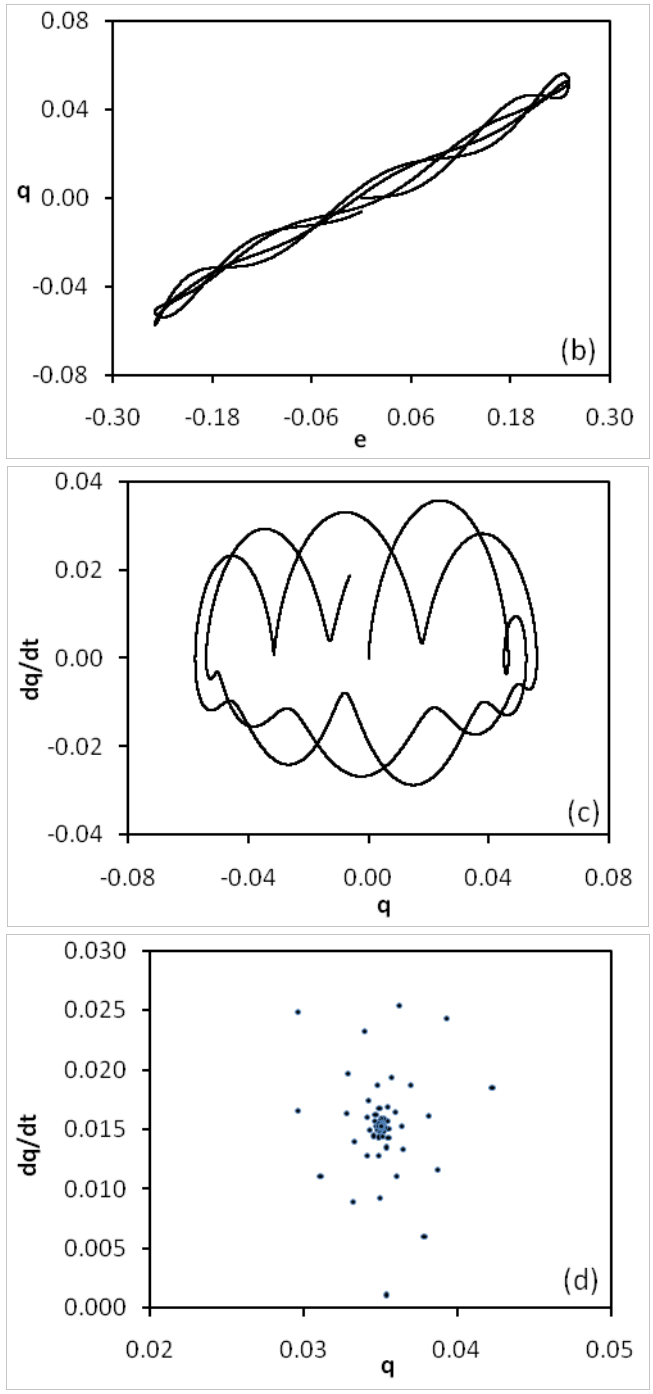

Fig. 10. AFE phase diagrams when $\omega = 3.0\ \omega_0$, and $e_0 = 0.6\ e_C$

Conclusion

From the results, i. e., the coupled oscillatory Equations of motion (8), and the numerically generated curves in Figures 2 to 10, the AFE system, i. e., ADP, in its first ordered phase exhibits high sensitivity to changes of initial conditions in frequencies and amplitudes of the applied electric field. This is due to the existence of nonlinear third and fifth order terms in Equations (8). As the amplitude of field slightly increases, the system exhibits quasi-periodicity with period multiplications on top of the applied frequencies. This feature is obvious in Figures 3 to 5, with the wavy structures on the slightly distorted patterns of q versus s, and q versus e curves. As the amplitude of applied field increases further, the system loses its periodicity, or the responses of the system become aperiodic, as shown in Figures 5 to 7. When the amplitude of applied field is extremely high, the system exhibits apriodic chaotic responses as shown in Figures 8. The main mechanism for the changes of responses of the AFE system from

periodic to quasi-periodic, to aperiodic, and to aperiodic chaotic, corresponding to the increases in amplitudes of the applied electric fields in Figures 2 to 8, is mainly due to repeated stretching and folding (Strogatz 2018) of the responses of the AFE system to the applied electric field.

The theoretical and numerical approaches here manage to unravel parts of the nonlinear and chaotic responses of the AFE systems, i. e., ADP, with respect to changes in frequency and amplitude of the applied electric field. The model described in this paper can be applied to other first order AFE which can be formulated by the same approaches. The results of nonlinear and chaotic responses using this approach can be further used to determine the transmission and reflection of optical waves through films and multilayers of nonlinear medium (Goldstone, Garmire 1984). This is an alternative to the conventional approach in derivations of nonlinear susceptibility tensors using series expansion of polarization in terms of electric fields, e. g. $P = \varepsilon_0\chi^{(1)} E + \varepsilon_0\chi^{(2)} EE + \varepsilon_0\chi^{(3)} EEE$, and use the results in the derivations of linear and nonlinear dielectric functions (Murgan et al. 2002).

Conflict of Interest

The author declares that there is no conflict of interest, either existing or potential.

References

Chan, T. Y. (2010) *Study of chaotic dynamics and hysteresis in bulk antiferromagnet and Antiferromagnetic Film. MSc Thesis (Antiferromagnetism)*. George Town, Universiti Sains Malaysia, 125 p. (In English)

Diestelhorst, M. (2003) What can we learn about ferroelectrics using methods of nonlinear dynamics? *Condensed Matter Physics*, 6 (2), 189–196. https://doi.org/10.5488/CMP.6.2.189 (In English)

Goldstone, J. A., Garmire, E. (1984) Intrinsic optical bistability in nonlinear media. *Physical Review Letter*, 53 (9), 910–913. https://doi.org/10.1103/PhysRevLett.53.910 (In English)

Ledzion, R., Bondarczuk, K., Kucharczyk, W. (2004) Temperature dependence of the quadratic electrooptic effect andestimation of antipolarization of ADP. *Crystal Research and Technology*, 39 (2), 161–164. https://doi.org/10.1002/crat.200310165 (In English)

Lines, M. E., Glass, A. M. (1977) *Principles and applications of ferroelectrics and related materials*. Oxford: Clarendon Press, 664 p. (In English)

Milek, J. T., Neuberger, M. (1972) *Handbook of Electronic Materials. Vol.8. Linear electrooptic modular materials*. New York: IFI/Plenum Publ., 264 p. (In English)

Murgan, R., Tilley, D. R., Ishibashi, Y. et al. (2002) Calculation of nonlinear-susceptibility tensor components in ferroelectrics: Cubic, tetragonal, and rhombohedral symmetries. *Journal of the Optical Society of America B*, 19 (9), 2007–2021. https://doi.org/10.1364/JOSAB.19.002007 (In English)

Press, W. H., Teukolsky, S. A., Vetterling, W. T., Flannery, B. P. (1996) *Numerical recipes in C: The art of scientific computing*. 2nd ed. Cambridge: Cambridge University Press, 537 p. (In English)

Strogatz, S. H. (2018) *Nonlinear dynamics and chaos with applications to Physics, Biology, Chemistry, and Engineering*. New York: CRC Press, 532 p. https://doi.org/10.1201/9780429492563 (In English)

Tan, E. K. (2001) *Static and dynamic properties of ferroelectric materials. MSc Thesis (Ferroelectricity)*. George Town, Universiti Sains Malaysia, 164 p. (In English)

Toh, P. L. (2009) *Study of chaotic dynamics and hysteresis in bulk ferromagnet and ferromagnetic film based on yttrium iron garnet. MSc Thesis (Ferromagnetic Materials)*. George Town, Universiti Sains Malaysia, 76 p. (In English)

Physics of Semiconductors. Semiconductors

UDC 538.9 + 535.3

EDN QDEXBE
https://www.doi.org/10.33910/2687-153X-2022-3-3-137-143

Optical characteristics of modified $As_{30}S_{70}$ thin films

V. T. Avanesyan✉[1], P. S. Provotorov[1], M. Krbal[2], A. V. Kolobov[1]

[1] Herzen State Pedagogical University of Russia, 48 Moika Emb., Saint Petersburg 191186, Russia
[2] Center of Materials and Nanotechnologies, University of Pardubice,
95 Studentska Str., Pardubice 532 10, Czech Republic

Authors

Vachagan T. Avanesyan, ORCID: 0000-0001-5772-8375, e-mail: avanesyan@mail.ru

Pavel S. Provotorov, ORCID: 0000-0003-1117-5431, e-mail: p.provotorov95@yandex.ru

Milos Krbal, ORCID: 0000-0002-8317-924X

Alexander V. Kolobov, ORCID: 0000-0002-8125-1172, e-mail: akolobov@me.com

For citation: Avanesyan, V. T., Provotorov, P. S., Krbal, M., Kolobov, A. V. (2022) Optical characteristics of modified $As_{30}S_{70}$ thin films. *Physics of Complex Systems*, 3 (3), 137–143. https://www.doi.org/10.33910/2687-153X-2022-3-3-137-143
EDN QDEXBE

Received 18 April 2022; reviewed 6 June 2022; accepted 6 June 2022.

Funding: This work has been performed as part of the joint Russian-Czech project funded by Russian Foundation for Basic Research (grant 19-53-26017) and Czech Science Foundation (grant 20-23392J).

Abstract. The paper reports the results of a comparative study of optical properties of thin films of arsenic chalcogenides of the As–S system taking into account the effect of their modification with molybdenum. An analysis of the experimental optical transmission spectra made it possible to calculate the dispersion curves of the refractive, absorption, and extinction coefficients of the medium, as well as the real and imaginary components of the complex permittivity. The revealed features of the behavior of the obtained spectral dependences are associated with the stereoeffect of a lone electron pair (LEP) in the structure of the arsenic compound under study.

Keywords: arsenic sulfide, molybdenum, spin-coating, optical transmission

Introduction

Chalcogenide glassy semiconductors (ChGS) are of great interest due to their unique structural, electronic, and optical properties (Tsendin 1996). These compounds are being actively studied in connection with a number of potential applications, in particular, as materials with a phase transition effect in memory elements based on phase transitions and optoelectronic devices (Kolobov et al. 2014; 2015). One of the reasons for the lack of wide use of arsenic chalcogenides is the absence of complete information about the optical characteristics of films based on these substances, which are sufficiently dependent on the method and conditions of manufacture. These main characteristics, as a rule, include the spectral dependence of the transmission and absorption coefficients, as well as the nature of the dispersion of the components of the complex refractive index in the entire operating range of the spectrum. Accurate determination of the optical constants of ChGS is also important for the development of promising technological processes and applications.

It should be noted that chalcogenide glasses are semiconductors with lone electron pair (LEP) in the chemical bond structure, the presence of which is one of the factors of glass formation (Bogoslovskiy, Tsendin 2012). In many chalcogenide semiconductors, a significant influence of the LEP on the anomalies of many of their parameters remains. It should also be noted that one of the reasons for the deviation

of the energy dependence of the absorption coefficient from strictly exponential is the presence of unshared electron pairs in the ChGS structure. The interaction of LEP with the local environment is one of the main reasons for the formation of the corresponding states in the tails of energy bands (Kastner 1972), which play an active role in the manifestation of certain optical properties of the material.

Thin films based on arsenic sulfide doped with d-metals are promising polyfunctional media for the structural modification of ChGS as one of the ways to control the properties of a material by changing its structure without changing its chemical composition (Gutenev et al. 1989). Changes in the properties of the modified glass are due to the chemical nature of the introduced impurity, which, in the case of a transition metal, is stabilized in the glass in states with unsaturated chemical bonds, which leads to the appearance of impurity conductivity in such glass. The most significant impurities that determine optical losses in the transparency region of glasses are impurities of 3d transition metals (Lazukina, et al. 2020).

In this work, we study the optical properties of thin films of $As_{30}C_{70}$ ChGS modified with molybdenum, which is a d-element.

Experimental methods

Thin ChGS films of $As_{30}S_{70}$ composition were synthesized on a glass substrate using the spin-coating technology (Thi et al. 2017). The modifying component was molybdenum, the presence of which in the ChGS structure was provided by adding a chemical compound, ammonium tetrathiomolybdate $(NH_4)_2MoS_4$, dissolved in propylamine, to the solution containing the As–S system. The composition of the films was confirmed by *X*-ray diffraction. Using an SF-2000 type spectrometer in the spectral wavelength range λ = 400–1100 nm, the dependences of the transmittance $T(\lambda)$ of the absorbed light for the samples under study at room temperature were obtained. Other optical constants of the studied films were determined by calculation using standard methods.

Results and discussion

As the studies performed earlier (Provotorov et al. 2021) show, the observed shape of the optical transmission spectra $T(\lambda)$ (T is the transmittance, λ is the radiation wavelength) of samples of ChGS films is characteristic of the films of the system under study. It has been established that in the transparency region this spectral dependence is significantly distorted by interference phenomena in thin films due to multiple reflections of the incident radiation, which, in turn, may indicate the homogeneity of the synthesized film. From the experimental spectra $T(\lambda)$ of $As_{30}S_{70}$ thin films in the presence and in the absence of molybdenum impurity, the spectral dependences of a number of other optical constants were determined. The $T(\lambda)$ function is complex and largely dependent on the refractive index of the film, the refractive index of the substrate, and the wavelength of light.

The use of the well-known Swanepoel method (Swanepoel 1983), taking into account the interference effect, made it possible to determine the spectral dependences of the refractive index, the dispersion of which was determined by the relation:

$$n(\lambda) = \sqrt{N + \sqrt{N^2 - s^2}} \quad (1)$$

There,

$$N = \frac{2s(T_M - T_m)}{T_M T_m} + \frac{s^2 + 1}{2}, \quad (2)$$

T_M and T_m are the values of the maxima and minima of the spectral dependence of the transmittance at the corresponding wavelength and s is refractive index of the substrate.

The parameter s, taking into account the dispersion of its transmittance T_s (λ), was found from the expression (Aly 2009):

$$s = \frac{1}{T_s} + \sqrt{\frac{1}{T_s^2} - 1}. \quad (3)$$

 https://www.doi.org/10.33910/2687-153X-2022-3-3-137-143

In the region of strong absorption, interference effects disappear, and the curves $T_M(\lambda)$ and $T_m(\lambda)$ at $\lambda < 550$ nm converge to common curves (envelopes) for samples of both types (Fig. 1 and Fig. 2). Here $T_g(\lambda) = \sqrt{T_M(\lambda) T_m(\lambda)}$ is the geometric mean value of the transmittance.

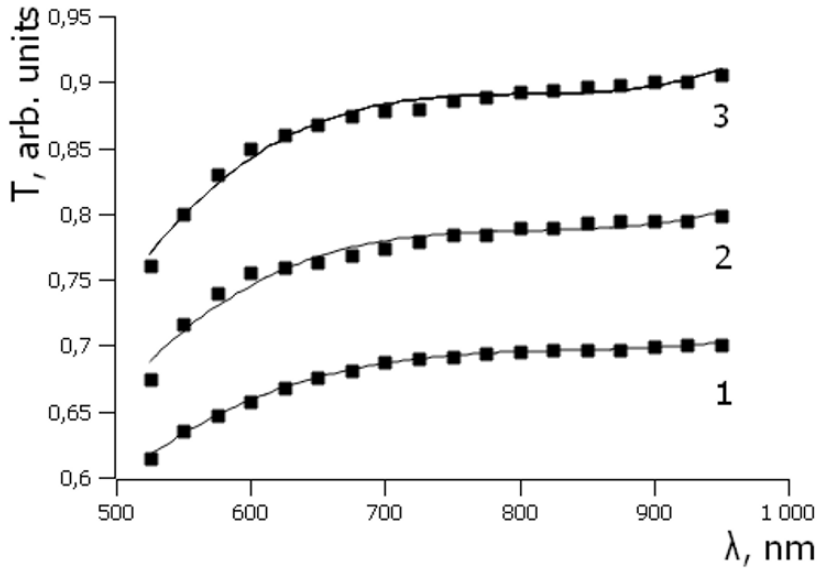

Fig. 1. Transmission spectra of the $As_{30}S_{70}$ film: 1—$T_m(\lambda)$, 2—$T_g(\lambda)$, 3—$T_M(\lambda)$

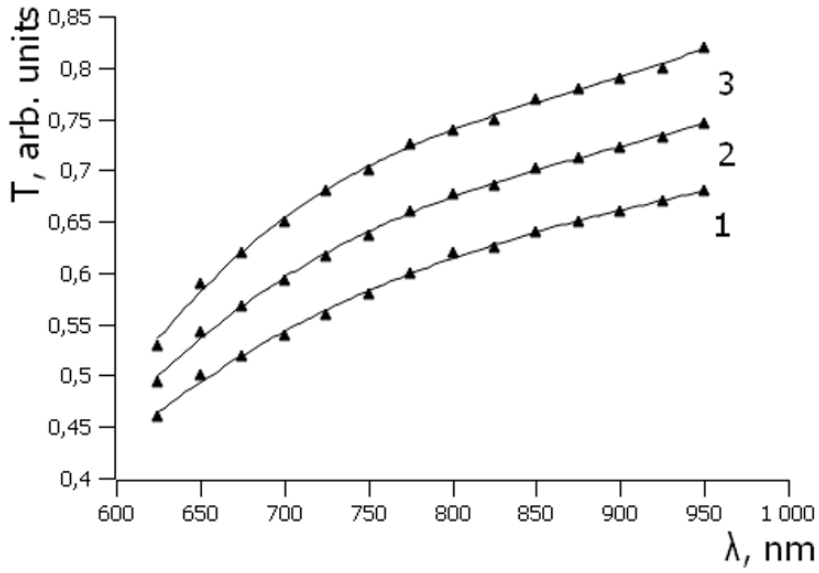

Fig. 2. Transmission spectra of the $As_{30}S_{70}$:Mo film: 1—$T_m(\lambda)$, 2—$T_g(\lambda)$, 3—$T_M(\lambda)$

It follows from the presented data that the transmission spectra are shifted toward a longer wavelength upon modification. Figure 3 shows the dispersion dependences of the refractive index for different compositions of the samples under study, calculated by Formula (2). The data indicate the presence of a dispersion of the refractive index with an increase in its values in the short-wavelength region. As the wavelength increases, the value of the refractive index decreases, indicating that the material under study exhibits normal behavior of dispersion characteristics.

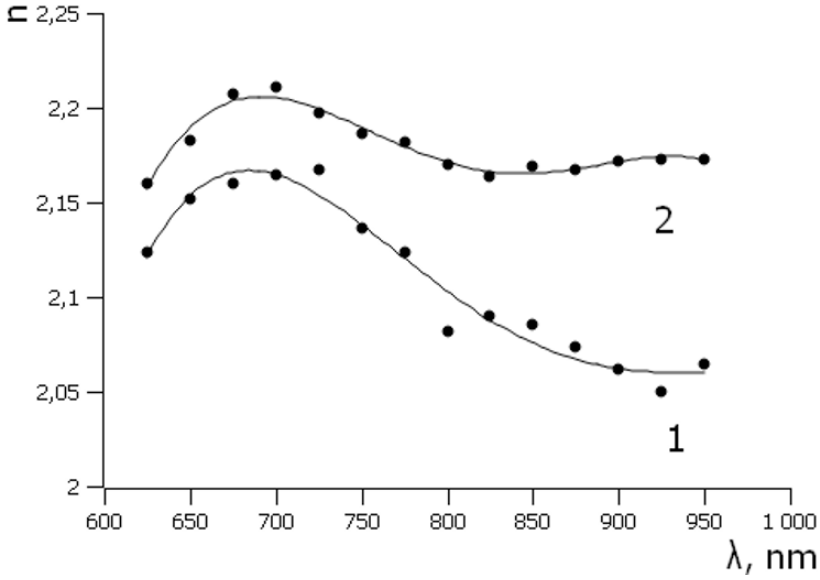

Fig. 3. Refraction spectra of the $As_{30}S_{70}$:Mo (1) and $As_{30}S_{70}$ (2) films

A sharper decrease in the index takes place in a sample of the modified As-S:Mo film, which, in turn, can be explained by an increment of transmission in the region of long wavelengths. The growth of refractive index may mean an increase in the polarizability of the material under study. The spectral dependence of the refractive index makes it possible to estimate the thickness of ChGS films, the value of which, taking into account the basic equation for interference fringes, can be determined as follows (Sharma, Katyal 2007):

$$d = \frac{\lambda_1 \lambda_2}{2\left(\lambda_1 n_2 - \lambda_2 n_1\right)}, \tag{4}$$

here n_1 and n_2 are the refractive indices for two adjacent maxima or minima at wavelengths λ_1 and λ_2. As a result of the performed analysis, the thickness of the studied film was calculated to be $d \approx 850$ nm.

Figure 4 shows the absorption coefficient spectra $\alpha(\lambda)$ obtained using the well-known relation $\alpha = -\ln T/d$.

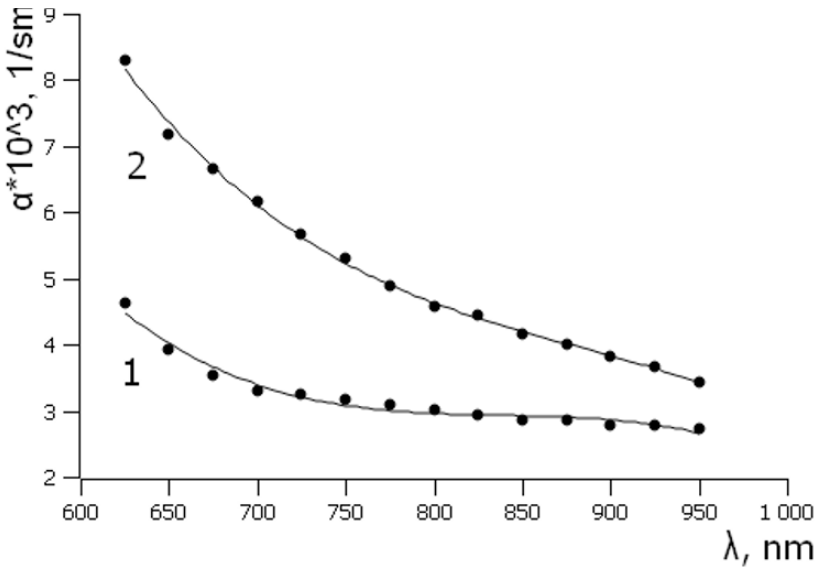

Fig. 4. Absorption spectra of the $As_{30}S_{70}$ (1) and $As_{30}S_{70}$:Mo (2) films

 https://www.doi.org/10.33910/2687-153X-2022-3-3-137-143

The presented experimental data indicate an increase in the value of the absorption coefficient for the modified films and, consequently, a decrease in their transparency. The obtained dependences made it possible to pass to the dispersion curves of the imaginary component of the complex refractive index $n^* = n - ik$ (here, extinction coefficient $k(\lambda) = \alpha\lambda/4\pi$) (Fig. 5).

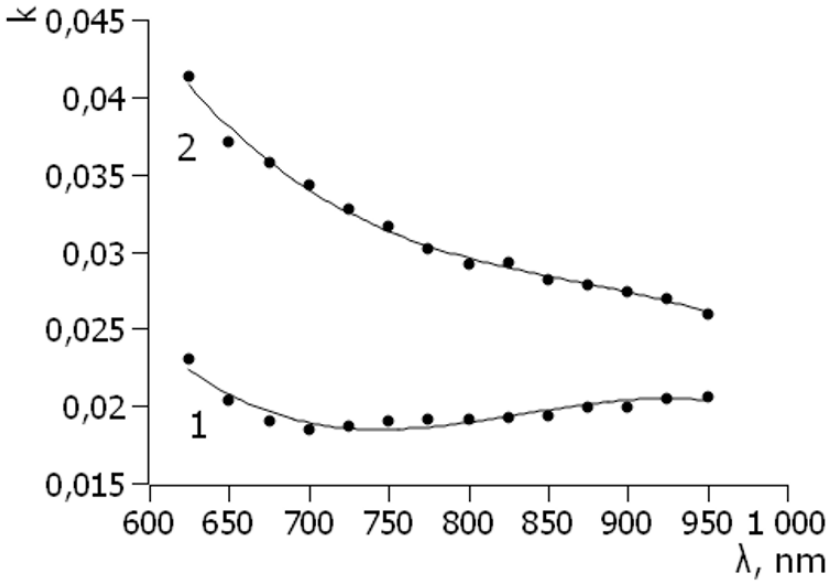

Fig. 5. Extinction coefficient spectra of the $As_{30}S_{70}$ (1) and $As_{30}S_{70}$:Mo (2) films

This coefficient gives information about the interaction of the material with the electric field of electromagnetic radiation and characterizes the attenuation of oscillations in the amplitude of the electric field strength. Studying the behavior of this parameter is important for the development of photonics devices. A decrease in the value of this coefficient for an unmodified film with increasing wavelength shows that part of its light flux is lost due to scattering and absorption.

Figure 6 shows the calculated dispersion dependences for the real component $\varepsilon' = n^2 - k^2$ of the complex permittivity $\varepsilon^* = \varepsilon' - i\varepsilon''$. The function $\varepsilon'(\lambda)$ characterizes the dispersion of an electromagnetic wave propagating deep into the substance, and the spectral dependence of the imaginary component $\varepsilon'' = 2nk$ (Fig. 7) is related to the absorption of the electric field energy during the orientation of charge formations. From the data shown in Figs. 6 and 7, it follows that both the real and imaginary parts of ε^* experience a constant increase with increasing photon energy, and it is sharper for the modified sample.

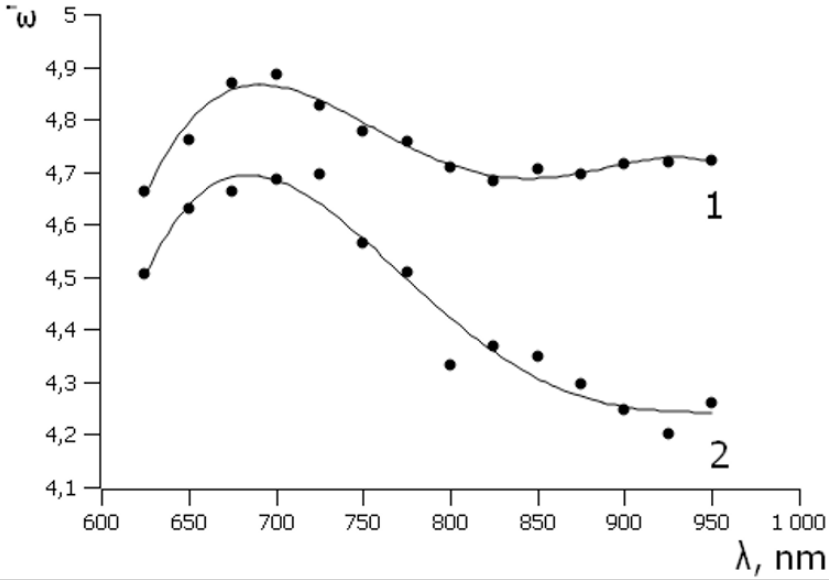

Fig. 6. Real permittivity spectra of the $As_{30}S_{70}$ (1) and $As_{30}S_{70}$:Mo (2) films

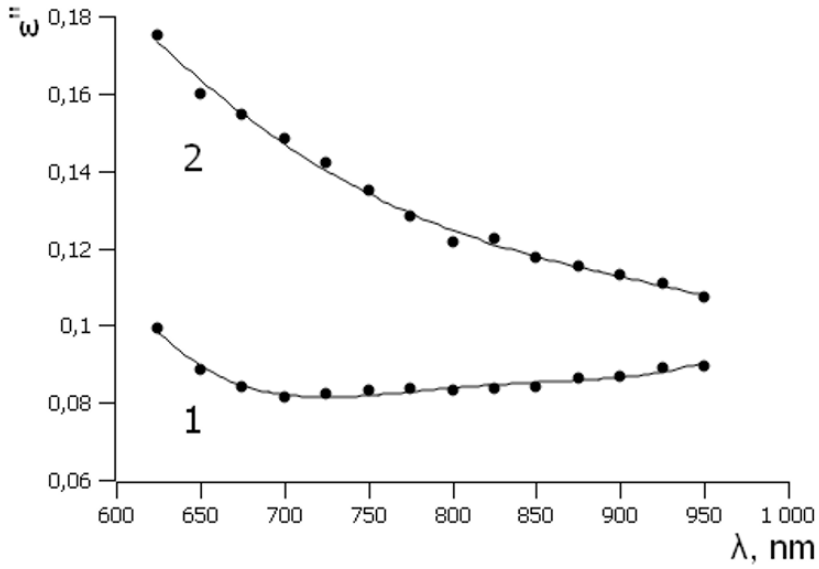

Fig. 7. Imaginary permittivity spectra of the $As_{30}S_{70}$ (1) and $As_{30}S_{70}$:Mo (2) films

It has been established that the main physical and, in particular, optical properties of chalcogenide glasses are largely associated with the presence of the LEP of chalcogens, which take part in the formation of the top of the valence band of the semiconductor (Nalwa 2000). It was found that the appearance of impurity centers in ChGS as a result of modification cannot have a significant effect on the stereochemical activity of these pairs, whose electron excitation is mainly responsible for photostructural transformations. The interaction of electrons of a lone pair of different atoms with each other and with the local environment can lead to an expansion of the spectrum of localized states in the band gap in ChGS (Meden, Sho 1991).

Conclusion

The optical transmission spectra of thin films of the chalcogenide glassy semiconductor $As_{30}S_{70}$ in the wavelength range 400–1000 nm with and without molybdenum impurities at room temperature are studied. Taking into account the observed interference effects, the envelope method was used to determine the thickness of the studied thin-film structures and the dispersion of the refractive index. In the investigated spectral range, the dispersion dependences of the optical constant, i. e., the absorption and refraction indices, as well as the components of the complex permittivity, were determined. The influence of the modifying factor on the optical properties of thin films of the glassy compound $As_{30}S_{70}$ has been established. The essential role of the presence of stereochemically active lone pairs of chalcogen electrons in the structure of the chemical bond is described. The results obtained in this work seem important for the search for and synthesis of new multicomponent film based on chalcogenide glassy materials for practical applications.

Conflict of Interest

The authors declare that there is no conflict of interest, either existing or potential.

Author contributions

Vachagan T. Avanesyan wrote the article and conducted experiments; Pavel S. Provotorov conducted experiments; Milos Krbal made samples; Alexander V. Kolobov prepared the discussion of results. All the authors discussed the final work.

References

Aly, K. A. (2009) Optical properties of Ge–Se–Te wedge-shaped films by using only transmission spectra. *Journal of Non-Crystalline Solids*, 355 (28–30), 1489–1495. https://doi.org/10.1016/j.jnoncrysol.2009.05.042 (In English)

Bogoslovskiy, N. A., Tsendin, K. D. (2012) Fizika effektov pereklyucheniya i pamyati v khal'kogenidnykh stekloobraznykh poluprovodnikakh [Physics of switching and memory effects in chalcogenide glassy semiconductors]. *Fizika i tekhnika poluprovodnikov*, 46 (5), 577–608. (In Russian)

Gutenev, M. S., Tver'yanovich, Yu. S., Krasil'nikova, A. P., Kochemirovskij, V. A. (1989) Dielektricheskaya spektroskopiya khal'kogenidnykh stekol, legirovannykh perekhodnymi metallami [Dielectric spectroscopy of chalcogenide glasses doped with transition metals]. *Fizika i khimiya stekla*, 15 (1), 84–90. (In Russian)

Kastner, M. (1972) Bonding bands, lone-pair bands, and impurity states in chalcogenide semiconductors. *Physical Review Letters*, 28 (6), 355–357. https://doi.org/10.1103/PhysRevLett.28.355 (In English)

Kolobov, A. V., Fons, P., Tominaga, J. (2014) Athermal amorphization of crystallized chalcogenide glasses and phase-change alloys. *Physica Satus Solidi (B)*, 251 (7), 1297–1308. https://doi.org/10.1002/pssb.201350146 (In English)

Kolobov, A. V., Fons, P., Tominaga, J. (2015) Understanding phase-change memory alloys from a chemical perspective. *Scientific Reports*, 5 (1), article 13698. https://doi.org/10.1038/srep13698 (In English)

Lazukina, O. P., Malyshev, K. K., Volkova, E. N., Churbanov, M. F. (2020) Primesnyj sostav obraztsov vysokochistykh stekol Vystavki-kollektsii veshchestv osoboj chistoty [Impurity composition of samples of high-purity glasses Exhibition-collection of substances of high purity]. *Neorganicheskie materialy*, 56 (4), 429–437. https://doi.org/10.31857/S0002337X20040077 (In Russian)

Meden, A., Sho, M. (1991) *Fizika i primenenie amorfnykh poluprovodnikov [Physics and applications of amorphous semiconductors]*. Moscow: Mir Publ., 670 p. (In Russian)

Nalwa, H. S. (2000) *Handbook of advanced electronic and photonic materials and devices: In 10 vols. Vol. 1*. London: Academic Press, 356 p. (In English)

Provotorov, P. S., Avanesyan, V. T., Krbal, M., Kolobov, A. V. (2021) Effect of doping of molybdenum on the optical properties of glasses of the As-S system. *Physics of Complex Systems*, 2 (3), 115–121. https://doi.org/10.33910/2687-153X-2021-2-3-115-121 (In English)

Sharma, P., Katyal, S. C. (2007) Determination of optical parameters of a-$(As_2Se_3)_{90}Ge_{10}$ thin film. *Journal of Physics D: Applied Physics*, 40 (7), article 2115. https://doi.org/10.1088/0022-3727/40/7/038 (In English)

Swanepoel, R. (1983) Determination of the thickness and optical constants of amorphous silicon. *Journal of Physics E: Scientific Instruments*, 16 (12), article 1214. https://doi.org/10.1088/0022-3735/16/12/023 (In English)

Thi, H. N., Tekshina, E. V., Lazarenko, P. I. et al. (2017) Tonkie plenki binarnykh khal'kogenidov As_2X_3 (X = S, Se), poluchennye metodom spin-koatinga [Thin films of binary chalkogenides As_2X_3 (X = S, Se) prepared by spin coating method]. *Rossijskij tekhnologicheskij zhurnal — Russian Technological Journal*, 5 (3), 51–57. https://doi.org/10.32362/2500-316X-2017-5-3-51-57 (In Russian)

Tsendin, K. D. (ed.). (1996) *Elektronnye yavleniya v khal'kogenidnykh stekloobraznykh poluprovodnikakh [Electronic phenomena in chalcogenide glassy semiconductors]*. Saint Petersburg.: Nauka Publ., 485 p. (In Russian)

Physics of Semiconductors. Semiconductors

UDC 538.9 + 535.3

EDN RVKOKJ
https://www.doi.org/10.33910/2687-153X-2022-3-3-144-148

Nernst mobility of holes in Bi_2Te_3

S. A. Nemov✉[1], G. V. Demyanov[1], A. V. Povolotskiy[2]

[1] Peter the Great Saint Petersburg Polytechnic University,
29 Polytechnicheskaya Street, Saint Petersburg 195251, Russia
[2] Saint Petersburg State University, 7/9 Universitetskaya Emb., Saint Petersburg 199034, Russia

Authors
Sergey A. Nemov, ORCID: 0000-0001-7673-6899, e-mail: nemov_s@mail.ru
Grigorij V. Demyanov, e-mail: demyanov.g@bk.ru
Alexey V. Povolotskiy, e-mail: apov@inbox.ru

For citation: Nemov, S. A., Demyanov, G. V., Povolotskiy, A. V. (2022) Nernst mobility of holes in Bi_2Te_3. *Physics of Complex Systems*, 3 (3), 144–148. https://www.doi.org/10.33910/2687-153X-2022-3-3-144-148 EDN RVKOKJ
Received 1 June 2022; reviewed 6 June 2022; accepted 6 June 2022.
Funding: The study did not receive any external funding.

Abstract. This paper presents the results of a study of the electrical conductivity coefficient, the Hall coefficient, the Seebeck coefficient, the transverse Nernst-Ettingshausen coefficient and their anisotropy in a Bi_2Te_3 single crystal with a hole concentration $p = 1 \times 10^{10–19}$ cm^{-3} at temperatures 77–350 K. It is established that hole scattering occurs mainly on long-wave acoustic phonons. Despite the fact that the chemical potential level is located near the top of the additional extreme of the valence band, no interband scattering was detected. The complex structure of the valence band is confirmed.

Keywords: Bismuth telluride, hole conductivity, temperature dependence, specific electrical conductivity, thermopower coefficient, Hall coefficient, Nernst-Ettingshausen coefficient, hole scattering mechanism, Nernst mobility, acoustic phonons

Introduction

Currently, there is an unusual situation with the interpretation of experimental data on the transport phenomena in hole chalcogenides of elements V of group V of the Mendeleev table $Bi_{1-x}Sb_xTe_{1-y}Se_y$, including in Bi_2Te_3. Single-band and double-band models are used to describe experimental data on transport phenomena in the temperature range of 100–600 degrees Celsius. For example, at temperatures above room temperature, minor carriers are also taken into account.

On the one hand, temperature dependences of the coefficients of specific electrical conductivity (σ) and thermopower (α) do not have any features and have the form typical for strongly doped semiconductors. The electrical conductivity decreases according to the law $\sigma \sim T^{-n}$, $n \approx 1.7$, and the thermopower is proportional to the temperature $\alpha \sim T$.

Such dependences σ (T) and α (T) are well described by a single-band model at temperatures of 77–300 K with the participation of one class of current carriers in the transport phenomena. This model is convenient for estimating the fundamental parameters of the band structure, determining the dominant scattering mechanisms, and calculating the thermoelectric properties of material (Goltsman et al. 1972; Lukyanova et al. 2005).

On the other hand, there is a significant increase in the Hall coefficient R(T) with temperature, which is traditionally associated in semiconductor physics with the redistribution of holes between two non-equivalent extremes of the valence band. Thus, such a dependence of R(T) indicates a complex structure

of the valence band and the participation of several types of current carriers in the transport phenomena. In this case, the calculations usually use a two-band model with two types of holes with different effective masses m^*_1 and m^*_2, respectively.

It should also be noted that most of the previous studies of transport phenomena were not comprehensive. They were carried out on poly-crystal samples and had a practical orientation.

Considering the practical significance of solid solutions $Bi_{1-x}Sb_xTe_{1-y}Se_y$, which are the main components of materials used in thermoelectric energy converters, operating in the temperature range of 200–600 K it is is advisable to continue studying the electrophysical properties of crystals of these materials and, first of all, the main component Bi_2Te_3.

Experiment

In the present work, studies of the kinetic coefficients were carried out on a single crystal grown by the Czochralski method with a Hall hole concentration $p = 1 \times 10^{10-19}$ cm^{-3}. The choice of the crystal is due to the fact, that, according to quantum oscillation data, the chemical potential level μ at 4.2 K at such a hole concentration is located near the additional extreme of the valence band, in this case $\mu \approx \Delta E_v \approx 0.03$ эВ, where ΔE_v is the energy gap between the peaks of the nonequivalent bands (Sologub et al. 1975). In this case, if the two-band model of the valence band is valid, we can expect the manifestation of features in the kinetic coefficients and, first of all, in the transverse Nernst–Ettingshausen effect, related to the interband scattering of "light holes" during their transition to additional extrema at low temperatures ($T \geq 77$ K).

In this paper, the temperature dependences of the main kinetic Hall (R), electrical conductivity (σ), thermopower (α), and the transverse Nernst–Ettingsgazuen (Q) coefficients and their anisotropy in the temperature range 77–350 K were measured. The obtained values of the coefficients R, σ, and α and their temperature dependences almost coincided with the literature data for samples with close Hall hole concentrations. Their values used in calculations are shown in Table 1.

Table 1. Basic kinetic coefficients of the p-Bi_2Te_3 crystal

	T, K	σ_{11}, Om^{-1}cm^{-1}	R_{123}, cm^3/C	α_{11}, mcV/K	$\frac{Q_{123}}{k_0/e}, \frac{\text{cm}^{-2}}{V \times s}$	x < 0	r
1	100	4800	0.38	50	–450	–0.427	0.051
2	150	2600	0.45	90	–451	–0.370	0.094
3	200	1600	0.52	140	–400	–0.297	0.157
4	250	1100	0.56	180	–280	–0.218	0.230
5	300	800	0.54	205	–140	–0.137	0.319
6	350	500	0.38	202	–10	–0.225	0.323

Temperature dependences of two components of the Nernst–Ettingsgazuen tensor Q_{123} and Q_{132} are shown in Figure 1.

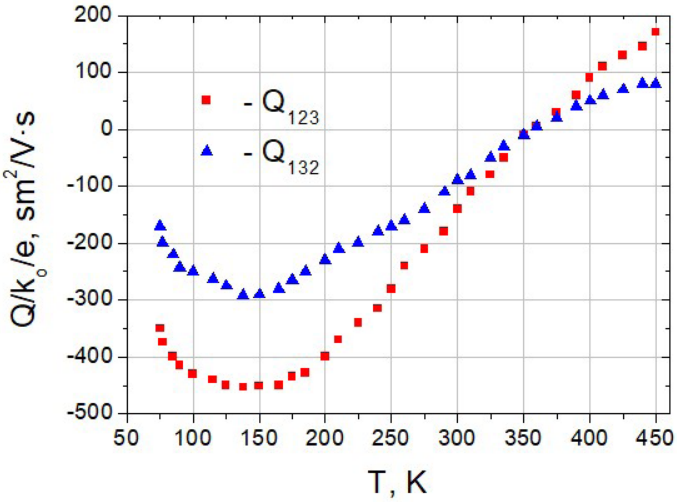

Fig. 1. Temperature dependence of the Nernst–Ettingsgazuen coefficient for a Bi_2Te_3 crystal$_2Te_3$ with a hole concentration *of* $1 \times 10^{10-19}$ *cm*$^{-3}$.

Note that the thermopower coefficient is isotropic and increases linearly with the temperature in the range of 85–250 K. The differences in the values of the Seebeck coefficients in the cleavage plane (α_{11}) and along the inversion-rotation axis $\bar{3}$ (α_{33}) are several MV/K, which does not exceed the measurement error. This result indicates that there is no noticeable anisotropy in the energy dependence of the hole relaxation time $\tau(\varepsilon)$ in Bi_2Te_3.

Discussion of experimental data

First of all, we note that measuring the four main kinetic coefficients R, σ, α, Q and their temperature dependences allows us to determine the main parameters of the band and structure of semiconductors, as well as the dominant scattering mechanisms in a single-band model (Zhitinskaya et al. 1966), and to conduct a correct analysis of experimental data for several types of current carriers.

Let us take a closer look at the obtained data. Let us start with the Hall effect. Both components of the Hall coefficient tensor R_{123} and R_{132} in hole chalcogenide materials $Bi_{1-x}Sb_xTe_{1-y}Se_y$ (including in Bi_2Te_3) (Goltsman et al. 1972; Sologub et al. 1975) grow with increasing temperature. Therefore, in the materials of group $A_2^{V}B_3^{VI}$, it is customary to determine the concentration of holes p from the larger component of the Hall tensor R_{77} at a temperature of 77 K. In p-Bi_2Te_3 there is a large component of the Hall tensor R_{132}. The concentration of holes is calculated by the formula

$$p = \left(eR_{77}\right)^{-1} \tag{1}$$

The concentration determined in this way is called the Hall concentration of holes and is used in all calculations of the parameters of the zone structure.

Note that Formula (1) does not take into account the hall factor associated with the anisotropy of the effective mass (it is approximately 0.7–0.8 for the coefficient R_{132} in p-Bi_2Te_3 (Goltsman et al. 1972). Thus, the real concentration of holes is about 20–30% more.

The Bi_2Te_3 single crystals studied by us had a Hall concentration of holes $p \approx 1 \times 10^{19}$ cm^{-3}, the maximum was observed in unalloyed bismuth telluride crystals obtained by deviation from the stoichiometric composition (Goltsman et al. 1972).

Our data on the Hall effect are consistent with the literature data (Goltsman et al. 1972). Both components of the Hall tensor R_{123} and R_{132} grow with increasing temperature from the value of R_{77} to R_{300} (at room temperature) by about 1.4 times.

Let us discuss in more detail the data on the Nernst–Ettingshausen transverse effect, which are presented in Figure 1 as a temperature dependence of the Nernst–Ettingshausen coefficient Q divided by a multiplier k_0/e (where k_0 is the Boltzmann constant, e is the electron charge modulus).

In this form, experimental data on the Nernst–Ettingshausen transverse effect are usually presented. The fact is that the coefficient $Q/(k_0/e)$ has a dimension of $cm^2/V{\cdot}s$, and its module is called the Nernst mobility. In such units of measurement, it is convenient to compare the Nernst and Hall mobility (Rσ).

As can be seen from Figure 1, both components of the Nernst–Ettingsgazuen tensor Q_{123} and Q_{132} are negative at $T \le 350$ K. This means that in the studied temperature range according to the formula for Q, valid for degenerate statistics

$$Q = \frac{k_0}{e} R\sigma \frac{\pi^2}{3} \frac{k_0 T}{\mu} \left.\frac{\partial \ln \tau}{\partial \ln \varepsilon}\right|_{\varepsilon=\mu}. \tag{2}$$

So, the energy dependence of the relaxation time of holes $\tau(\varepsilon)$ is a function decreasing with energy ε. This dependence has only two mechanisms of current carriers scattering: on acoustic phonons and interband scattering.

Note that the idea of interband scattering was introduced by N. V. Kolomoets (Zhitinskaya et al. 1966). The inclusion of this mechanism of hole scattering in samples with a chemical potential located near the top of the additional extremum of the valence band, that is, under the condition of $\mu \approx \Delta E_v$ in the region of nitrogen temperatures, can lead to features in the temperature dependence of the Nernst mobility. The fact that the interband scattering is characterized by the large negative value of the derivative $\left.\frac{\partial \ln \tau}{\partial \ln \varepsilon}\right|_{\varepsilon=\mu}$,

 https://www.doi.org/10.33910/2687-153X-2022-3-3-144-148

as the relaxation time of "light" holes from the main extremum, in this case it is described by the expression according to (Kolomoets 1966):

$$\tau^{-1}(\varepsilon) = \tau_0^{-1} \begin{cases} \sqrt{\varepsilon}\ by\ \varepsilon < \Delta E_v \\ \sqrt{\varepsilon} + w_{12}\sqrt{\varepsilon - \Delta E_v}\ by\ \varepsilon > \Delta E_v \end{cases}, \tag{3}$$

where τ_0 is a constant coefficient in expression for the relaxation time of light holes when scattering by acoustic phonons $= \tau_0 \varepsilon^{-0,5}$; $w_{12} = \left(m_2^* / m_1^*\right)^{3/2} \left(\Xi_{12} / \Xi_{11}\right)^2$ is a parameter characterizing the probability of an interband transition of holes from the main to the additional extremum; m_1^* and m_2^* are the effective masses of the density of the states of holes in the first and second zones; Ξ_{11} and Ξ_{12} are the constants of the deformation potential for intraband and interband scattering of holes. Using the data on the four kinetic coefficients R, σ, α and Q, we will estimate the scattering parameter r, which is included in the expressed $\tau = \tau_0\, \varepsilon^{r-0,5}$ as part of a single-band model. Since the coefficients α and Q are equal, respectively

$$\alpha = \frac{k_0}{e}\frac{\pi^2}{3}\frac{k_0 T}{\mu}(r+1), \tag{4}$$

$$Q = \frac{k_0}{e}\frac{\pi^2}{3}\frac{k_0 T}{\mu} R\sigma\left(r - \frac{1}{2}\right), \tag{5}$$

we get an expression for their relationship

$$\frac{Q_{123}}{\alpha_{11} R_{123} \sigma_{11}} = \frac{r - 1/2}{r+1}, \tag{6}$$

where index 3 means the direction along the trigonal axis $\overline{3}$.

Denoting the experimental values of the relation by x

$$\frac{Q_{123}}{k_0/e} : \frac{\alpha_{11}}{k_0 e} \times R_{123}\sigma_{11} = x \tag{7}$$

we obtain an equation for determining the scattering parameter r

$$r = \frac{0,5 + x}{1 - x}. \tag{8}$$

The value of r obtained from experimental data is shown in Table 1, from which it can be seen that in the low temperature region the parameter r is close to zero. This means that in bismuth telluride at temperatures of 77 K and above, hole scattering on long-wave acoustic phonons dominates (parameter r = 0) and there are no signs of the inclusion of a new interband hole scattering mechanism.

As can be seen from Table 1, the parameter r does not decrease, rather, it shows a slight increase. So, there are no large modulo negative values of the scattering parameter characteristic of the interband scattering of holes. Thus, interband hole scattering is inefficient in p-Bi_2Te_3.

Perhaps, this is due to the fact that the transfer phenomena involve holes with slightly different effective masses of the density of states $m_1^* \sim (0,5-0,6)\, m_0$ and $m_2^* \sim (0,9-1,2)\, m_0$, where m_0 is the mass of a free electron. Estimates of effective masses are made for the two-band model (Goltsman et al. 1972; Sologub et al. 1975). In addition, the thermal blurring of the Fermi distribution function k_0T is comparable to the energy gap ΔE_v in the two-band model and the chemical potential μ, which eliminates the features in the energy dependence of the relaxation time of holes. Theoretical calculations of Bi_2Te_3 performed from the first principles confirm the complex structure of the valence band (Scheidemantel et al. 2003).

In conclusion, we note that at temperatures T > 250 K, non-basic carriers (electrons) appear and, in accordance with the theory of kinetic phenomena, the Hall coefficients and thermal EMF decrease, and the electrical conductivity increases. The Nernst–Ettingshausen coefficient at the same time sharply decreases in modulus and at temperatures T = 350 K it changes its sign to positive.

Conclusion

Thus, as a result of studies of the specific electrical conductivity, Hall coefficients, Seebeck coefficients and the Nernst-Ettingshausen transverse effect on a single crystal p-Bi_2Te_3 at temperatures of 77–350 K, it was found that the dominant mechanism of hole scattering is the scattering by long-wave acoustic phonons.

Due to the location of the chemical potential level μ in the studied crystal with a hole concentration of 1×10^{19} sm^{-3} near the top of the additional extremum ($\mu = \Delta E_v$) interband scattering was expected, however, it was not detected. Perhaps this is due to the fact that the holes involved in the transfer phenomena have slightly different effective masses, and the amount of thermal blurring of the Fermi distribution function k0T is comparable to the values of μ and ΔE_v.

The observed deviations of the experimental data on kinetic coefficients from the calculation results in the single-band approximation are associated with the complex structure of the valence band and the participation in the transfer phenomena of several groups of current carriers with different effective masses.

Conflict of Interest

The authors declare that there is no conflict of interest, either existing or potential.

Author Contributions

The authors have made an equal contribution to the preparation of the text.

References

Goltsman, B. M., Kudinov, V. A., Smirnov, I. A. (1972) *Poluprovodnikovye termoelektricheskie materialy na osnove Bi_2Te_3 [Semiconductor thermoelectric materials based on bismuth telluride Bi_2Te_3]*. Moscow: Nauka Publ., 320 p. (In Russian)

Kolomoets, N. V. (1966) Vliyanie mezhzonnykh perekhodov na termoelektricheskie svojstva veshchestva [Influence of interband transitions on thermoelectric properties of matter]. *Fizika tverdogo tela*, 8 (4), 997–1003. (In Russian)

Lukyanova, L. N., Kutasov, V. A., Konstantinov, P. P. (2005) Effektivnaya massa i podvizhnost' v tverdykh rastvorakh p-$Bi_{2-x}Sb_xTe_{3-y}Se_y$ dlya temperatur < 300 K [Effective mass and mobility in solid solutions of p-$Bi_{2-x}Sb_xTe_{3-y}Se_y$ for temperatures < 300 K]. *Fizika tverdogo tela*, 47 (2), 224–228. (In Russian)

Scheidemantel, T. J., Ambrosch-Draxl, C., Thonhauser, T. et al. (2003) Transport coefficients from first-principles calculations. *Physical Review B*, 68 (12), article 125210. https://doi.org/10.1103/PhysRevB.68.125210 (In English)

Sologub, V. V., Parfenyev, R. V., Goletskaya, A. D. (1975) Struktura valentnoj zony tellurida vismuta [Structure of the valence band of bismuth telluride]. *Pis'ma v Zhurnal eksperimental'noj i teoreticheskoj fiziki — JETP Letters*, 21 (12), 711–715. (In Russian)

Zhitinskaya, M. K., Kaidanov, V. I., Chernik, I. A. (1966) O neparabolichnosti zony provodimosti tellurida svintsa [On the nonparabolicity of the conduction band of lead telluride]. *Fizika tverdogo tela*, 8 (1), 295–297. (In Russian)

Summaries in Russian / Информация о статьях на русском языке

Физика конденсированного состояния

ИССЛЕДОВАНИЕ РЕЛАКСАЦИИ ЗАРЯДА В КОРОНОЭЛЕКТРЕТАХ НА ОСНОВЕ СОПОЛИМЕРА П(ВДФ-ТФЭ)

Гороховатский Юрий Андреевич, Сотова Юлия Ильинична, Темнов Дмитрий Эдуардович

Аннотация

В данной работе предложено объяснение механизма поляризации в поле коронного разряда полимерных пленок сополимера поливинилиденфторида-тетрафторэтилена (П(ВДФ-ТФЭ)) с помощью метода термостимулированных токов деполяризации. Определено, что для достижения лучших электретных свойств ПВДФ поляризацию необходимо проводить в поле отрицательного коронного разряда. Было обнаружено, что в исследуемых объектах имеется два сорта полярных структур, отличных по значениям энергии активации и частотного фактора. С помощью комплексного применения традиционных методов обработки пиков термостимулированных токов деполяризации и численных методов были определены параметры полярных структур обоих сортов, обнаруженных в составе П(ВДФ-ТФЭ).

Ключевые слова: электретное состояние, поливинилиденфторид, тетрафторэтилен, термоактивационная спектроскопия, метод слабой регуляризации

Для цитирования: Gorokhovatsky, Yu. A., Sotova, Yu. I., Temnov, D. E. (2022) A study of charge relaxation in corona electrets based on P(VDF-TFE) copolymer. *Physics of Complex Systems*, 3 (3), 104–108. https://www.doi.org/10.33910/2687-153X-2022-3-3-104-108 EDN OCOMWG

ГАЗОРАЗРЯДНАЯ АКТИВАЦИЯ НОВЫХ УПАКОВОЧНЫХ КОМПОЗИТНЫХ ПЛЕНОК ИЗ ПОЛИ (МОЛОЧНОЙ КИСЛОТЫ)

Павлов Андрей Александрович, Камалов Алмаз Маратович, Борисова Маргарита Эдуардовна, Малафеев Константин Вадимович, Юдин Владимир Евгеньевич

Аннотация

В данной работе исследованы электрофизические свойства новых композиционных диэлектриков на основе полилактида. С целью улучшения электретных свойств в полилактид были добавлены наполнители: гидроксиапатит, повиаргол, углеродные нановолокна. В ходе выполнения работы получены данные о скорости спада электретной разности потенциалов на образцах, об их проводимости, а также относительной диэлектрической проницаемости. Проведены испытания на механическую прочность. Проанализировано влияние наполнителей на электрофизические и механические свойства полилактида. На основе полученных данных были выбраны наиболее подходящие концентрации наполнителей для композитов, которые планируется применять в качестве упаковки.

Ключевые слова: полилактид, электрет, композиционный материал, гидроксиапатит, Повиаргол, углеродные нановолокна

Для цитирования: Pavlov, A. A., Kamalov, A. M., Borisova, M. E., Malafeev, K. V., Yudin, V. E. (2022) Gas discharge activation of new poly(lactic acid) packaging composite films. *Physics of Complex Systems*, 3 (3), 109–116. https://www.doi.org/10.33910/2687-153X-2022-3-3-109-116 EDN PTWGYL

Теоретическая физика

СИЛЫ ВНЕ СТАТИЧЕСКОГО ПРЕДЕЛА ВО ВРАЩАЮЩЕЙСЯ СИСТЕМЕ КООРДИНАТ

Гриб Андрей Анатольевич, Вертоградов Виталий Дмитриевич, Федоров Иван Евгеньевич

Аннотация

В этой статье мы рассматриваем вращающуюся систему отсчета пространства-времени Минковского, чтобы описать силы инерции за пределами статического предела. Мы рассматриваем силы инерции внутри статического предела, чтобы найти классический аналог, а затем находим выраже-

ния для этих сил вне статического предела, где мы не можем рассматривать предел $\frac{v}{c} \to 0$. Показано, что в общем случае, если угловая скорость объекта Ω равна угловому моменту ω, то ускорение равно нулю. В случае ω ≠ Ω мы показываем, что ω – Ω является убывающей функцией r.

Ключевые слова: вращающаяся система отсчета, статический предел, сила инерции, геодезический, пространство-время Минковского

Для цитирования: Grib, A. A., Vertogradov, V. D., Fedorov, I. E. (2022) The forces outside the static limit in the rotating frame. *Physics of Complex Systems*, 3 (3), 117–121. https://www.doi.org/10.33910/2687-153X-2022-3-3-117-121 EDN PYVSES

ЧИСЛЕННОЕ МОДЕЛИРОВАНИЕ НЕЛИНЕЙНЫХ И ХАОТИЧЕСКИХ ОТКЛИКОВ В ОБЪЕМНЫХ АНТИСЕГНЕТОЭЛЕКТРИКАХ С ИСПОЛЬЗОВАНИЕМ ПАРАМЕТРА ДИГИДРОФОСФАТА АММОНИЯ

Лим Сью-Чу

Аннотация

В этой статье нелинейный и хаотический отклики объемных антисегнетоэлектриков рассматриваются феноменологически и численно. Первая упорядоченная фаза объемных антисегнетоэлектриков сформулирована путем применения вариационного исчисления к разложениям плотности свободной энергии Ландау объемных антисегнетоэлектриков. Динамические отклики антисегнетоэлектриков в приложенном переменном электрическом поле получали с помощью уравнения движения Ландау — Халатникова. Полученные динамические уравнения представляют собой два дифференциальных уравнения второго порядка с нелинейной связью, соответствующие двум взаимопроникающим подрешеткам антисегнетоэлектриков, и они решаются численно с использованием методов Рунге — Кутты четвертого порядка и параметров дигидрофосфата аммония в его первой упорядоченной фазе. Эти расчетные результаты представлены графически для различных частот и амплитуд в приложенных электрических полях.

Ключевые слова: антисегнетоэлектрики, дигидрофосфат аммония, хаос, плотность свободной энергии Ландау, нелинейность, сечения Пуанкаре

Для цитирования: Lim, S.-Ch. (2022) Numerical simulations of nonlinear and chaotic order parameter responses in bulk antiferroelectrics using ammonium dihydrogen phosphate parameter. *Physics of Complex Systems*, 3 (3), 122–136. https://www.doi.org/10.33910/2687-153X-2022-3-3-122-136 EDN QAMJZS

Физика полупроводников

ОПТИЧЕСКИЕ ХАРАКТЕРИСТИКИ МОДИФИЦИРОВАННЫХ ТОНКИХ ПЛЕНОК СОСТАВА $A_{S30}S_{70}$

Аванесян Вачаган Тигранович, Провоторов Павел Сергеевич, Крбал Милош, Колобов Александр Владимирович

Аннотация

Представлены результаты сравнительного исследования оптических свойств тонких пленок халькогенидов мышьяка системы As–S с учетом влияния их модификации молибденом. Анализ экспериментальных спектров оптического пропускания позволил расчетным путем вычислить дисперсионные кривые коэффициентов преломления, поглощения и экстинкции среды, а также действительную и мнимую составляющие комплексной диэлектрической проницаемости. Выявленные особенности поведения полученных спектральных зависимостей связаны со стереоэффектом неподеленной электронной пары (НЭП) в структуре исследуемого соединения мышьяка.

Ключевые слова: сульфид мышьяка, молибден, центрифугирование, оптическое пропускание

Для цитирования: Avanesyan, V. T., Provotorov, P. S., Krbal, M., Kolobov, A. V. (2022) Optical characteristics of modified $As_{30}S_{70}$ thin films. *Physics of Complex Systems*, 3 (3), 137–143. https://www.doi.org/10.33910/2687-153X-2022-3-3-137-143 EDN QDEXBE

НЕРНСТОВСКАЯ ПОДВИЖНОСТЬ ДЫРОК В Bi_2Te_3

Немов Сергей Александрович, Демьянов Григорий Владимирович, Поволоцкий Алексей Валерьевич

Аннотация

В настоящей работе представлены результаты исследования удельной электропроводности, коэффициента Холла, Зеебека, поперечного эффекта Нернста — Эттингсгаузена и их анизотропии в монокристалле Bi_2Te_3 с концентрацией дырок $p = 1 \cdot 10^{19}$ см$^{-3}$ при температурах 77–350 K. Установлено, что рассеяние дырок происходит в основном на длинноволновых акустических фононах. Несмотря на то, что уровень химического потенциала расположен вблизи вершины дополнительного экстремума валентной зоны, не обнаружено проявлений межзонного рассеяния. Подтверждено сложное строение валентной зоны.

Ключевые слова: Теллурид висмута, дырочная проводимость, температурная зависимость, удельная электропроводность, коэффициент термоЭДС, коэффициент Холла, коэффициент Нернста — Эттингсгаузена, механизм рассеяния дырок, нернстовская подвижность, акустические фононы

Для цитирования: Nemov, S. A., Demyanov, G. V., Povolotskiy, A. V. (2022) Nernst mobility of holes in Bi_2Te_3. *Physics of Complex Systems*, 3 (3), 144–148. https://www.doi.org/10.33910/2687-153X-2022-3-3-144-148 EDN RVKOKJ